ORGANOMETALLICS

Article

pubs.acs.org/Organometallics

Iridium and Ruthenium Complexes of *N*-Heterocyclic Carbene- and Pyridinol-Derived Chelates as Catalysts for Aqueous Carbon Dioxide Hydrogenation and Formic Acid Dehydrogenation: The Role of the Alkali Metal

Sopheavy Siek,[†] Dalton B. Burks,[†] Deidra L. Gerlach,[†] Guangchao Liang,[‡] Jamie M. Tesh,[†] Courtney R. Thompson,[†] Fengrui Qu,[†] Jennifer E. Shankwitz,[†] Robert M. Vasquez,[§] Nicole Chambers,[†] Gregory J. Szulczewski,[†] Douglas B. Grotjahn,*[,§] Charles Edwin Webster,*[,‡] and Elizabeth T. Papish*[,†]

[†]Department of Chemistry, The University of Alabama, Box 870336, Tuscaloosa, Alabama 35487-0336, United States

[‡]Department of Chemistry, Mississippi State University, Mississippi State, Mississippi 39762, United States

[§]Department of Chemistry and Biochemistry, San Diego State University, 5500 Campanile Drive, San Diego, California 92182-1030, United States

Supporting Information

ABSTRACT: Hydrogenation reactions can be used to store energy in chemical bonds, and if these reactions are reversible, that energy can be released on demand. Some of the most effective transition metal catalysts for CO_2 hydrogenation have featured pyridin-2-ol-based ligands (e.g., 6,6′-dihydroxybipyridine (6,6′-dhbp)) for both their proton-responsive features and for metal−ligand bifunctional catalysis. We aimed to compare bidentate pyridin-2-ol based ligands with a new scaffold featuring an *N*-heterocyclic carbene (NHC) bound to pyridin-2-ol. Toward this aim, we have synthesized a series of [Cp*Ir(NHC-py^{OR})Cl]OTf complexes where R = ^{t}Bu (**1**), H (**2**), or Me (**3**). For comparison, we tested analogous bipy-derived iridium complexes as catalysts, specifically [Cp*Ir(6,6′-dxbp)Cl]OTf, where x = hydroxy ($\mathbf{4}_{Ir}$) or methoxy ($\mathbf{5}_{Ir}$); $\mathbf{4}_{Ir}$ was reported previously, but $\mathbf{5}_{Ir}$ is new. The analogous ruthenium complexes were also tested using [(η^6-cymene)Ru(6,6′-dxbp)Cl]OTf, where x = hydroxy ($\mathbf{4}_{Ru}$) or methoxy ($\mathbf{5}_{Ru}$); $\mathbf{4}_{Ru}$ and $\mathbf{5}_{Ru}$ were both reported previously. All new complexes were fully characterized by spectroscopic and analytical methods and by single-crystal X-ray diffraction for **1**, **2**, **3**, $\mathbf{5}_{Ir}$, and for two [Ag(NHC-py^{OR})$_2$]OTf complexes **6** (R = ^{t}Bu) and **7** (R = Me). The aqueous catalytic studies of both CO_2 hydrogenation and formic acid dehydrogenation were performed with catalysts **1**−**5**. In general, NHC-py^{OR} complexes **1**−**3** were modest precatalysts for both reactions. NHC complexes **1**−**3** all underwent transformations under basic CO_2 hydrogenation conditions, and for **3**, we trapped a product of its transformation, $\mathbf{3}_{SP}$, which we characterized crystallographically. For CO_2 hydrogenation with base and dxbp-based catalysts, we observed that x = hydroxy ($\mathbf{4}_{Ir}$) is 5−8 times more active than x = methoxy ($\mathbf{5}_{Ir}$). Notably, ruthenium complex $\mathbf{4}_{Ru}$ showed 95% of the activity of $\mathbf{4}_{Ir}$. For formic acid dehydrogenation, the trends were quite different with catalytic activity showing $\mathbf{4}_{Ir} \gg \mathbf{4}_{Ru}$ and $\mathbf{4}_{Ir} \approx \mathbf{5}_{Ir}$. Secondary coordination sphere effects are important under basic hydrogenation conditions where the OH groups of 6,6′-dhbp are deprotonated and alkali metals can bind and help to activate CO_2. Computational DFT studies have confirmed these trends and have been used to study the mechanisms of both CO_2 hydrogenation and formic acid dehydrogenation.

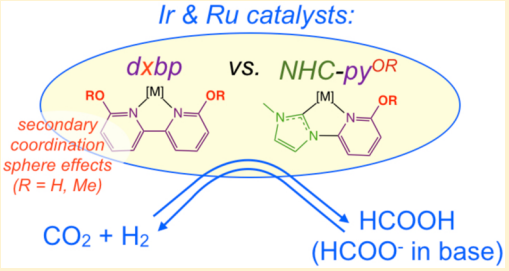

INTRODUCTION

Ligands that contain protic functional groups near the metal center can accelerate proton transfer events in many different types of reactions. Our research groups[1−4] and others[5,6] have pioneered the use of 6,6′-dihydroxybipyridine (6,6′-dhbp) ligands (Chart 1) for the formation of metal complexes that catalyze both oxidative and reductive reactions. The hydroxy groups near the metal center lead to a change in ligand charge upon deprotonation, and thereby, the electron density at the metal is altered. The ability to instantly modulate the character of the ligands and change from L_2 (6,6′-dhbp, neutral) to LX (monoanionic) and to X_2 (dianionic) can explain the catalytic rate enhancements that are seen upon deprotonation of the metal complexes.[2] Under oxidizing conditions, our group and others have shown that both iridium (e.g., $\mathbf{4}_{Ir}$[2] and its Ir-aqua analogue; Chart 1)[7,8] and copper complexes of 6,6′-dhbp undergo decomposition reactions in solution.[4] Furthermore, we

Received: October 22, 2016
Published: March 3, 2017

DOI: 10.1021/acs.organomet.6b00806
Organometallics 2017, 36, 1091−1106

Chart 1. Bidentate Ligands with Proximal Protic Functional Groups and Similar Metal Complexes in the Literature

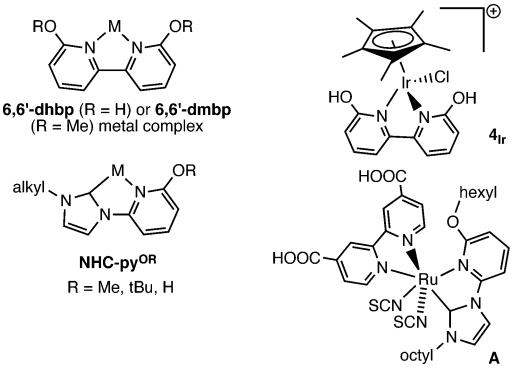

have also shown that Cu(II) complexes of 6,6′-dhbp undergo ligand loss at both high (>13) and low (<4) pH in aqueous solution.[4] Therefore, we had a strong interest in affixing a strong donor to the pyridinol ring to counteract the labile nature of the 6,6′-dhbp ligand.

Carbon dioxide hydrogenation is studied here because 6,6′-dhbp complexes and other pyridinol-based complexes of Ir(III) are especially effective at promoting this reaction and (de)hydrogenation in general.[6,9−11] Other highly efficient CO_2 hydrogenation homogeneous catalysts include several different iridium pincer complexes from Nozaki;[12] Brookhart and Meyer;[13] Bernskoetter, Hazari, and Palmore;[14] and others.[15] For formic acid dehydrogenation, a reusable highly active iridium catalyst with a P,N ligand was reported by Williams;[16] other groups have performed formic acid dehydrogenation in the course of methanol dehydrogenation.[17,18] Most of these (de)hydrogenation catalysts perform ionic hydrogenation, which is the sequential transfer of H^+ and H^-; other transition metal-based catalysts for ionic hydrogenation have been reported.[19−27]

The iridium(III) complexes based on 6,6′-dhbp and related ligands are noteworthy for how rapidly they catalyze both CO_2 hydrogenation and the reverse reaction.[6,11] The rate accelerations seen with 6,6′-dhbp have been attributed to electron donor ability, which is enhanced upon deprotonation and proximal OH/O- groups facilitating the transfer of H^+ via a metal−ligand bifunctional catalysis mechanism.[1,28−31] However, herein we have found that in some cases methoxy substituents are as effective as hydroxy groups at enhancing dehydrogenation rates. This is evident from comparing 6,6′-dhbp and 6,6′-dimethoxybipyridine (6,6′-dmbp) complexes of iridium and ruthenium. In addition, importantly, the role of alkali metals in hydrogenation reactions is elucidated for the first time with the 6,6′-dhbp scaffold.

N-Heterocyclic carbene (NHC) ligands are strong sigma donors that form stable metal−carbon bonds.[32−34] NHCs have been used in chelates before with pyridine rings (e.g., **A**; Chart 1),[35−37] including in Re, Mn, and Ni catalysts for electrochemical CO_2 reduction[38−41] but never with pyridinol as a protic ligand. We reasoned that a bidentate ligand containing an NHC and a pyridinol ring could offer a protic group on the metal center in the presence of a strong donor ligand (Chart 1, NHC-py^{OH}). These ligands could be tuned by deprotonation (producing OH/O- variants) while also containing strong metal carbon bonds. Herein, we report the NHC-py^{OH} ligand and related ethers, the Ir(III) complexes thereof, and the use of these new metal complexes toward the catalysis of CO_2 hydrogenation and the reverse dehydrogenation reaction.

RESULTS AND DISCUSSION

Synthesis and Characterization of the Ligands and the Metal Complexes. The *N*-heterocyclic carbene-pyridinol-derived ligands (NHC-py^{OR}) are easily synthesized as the OR = O^{t}Bu, OH, or OMe derivatives wherein O^{t}Bu serves as a protected form for making the OH derivatives. After chelation with the desired metal, moderate heat can drive the deprotection of the *t*-butyl group to produce the hydroxy-substituted ligand with the elimination of isobutene. OR = OMe is a control for comparison of hydrogen bond donor (OH) vs hydrogen bond acceptor (OMe) properties of the ligand.

Treating 2,6-difluoropyridine with excess sodium alkoxide (NaO^{t}Bu or NaOMe)[42−44] afforded 2-fluoro-6-alkoxypyridines with replacement of only one fluoride (Scheme 1). Further

Scheme 1. Synthesis of the Imidazolium Precursors to the NHC-py^{OR} Ligands (R = tBu, Me)

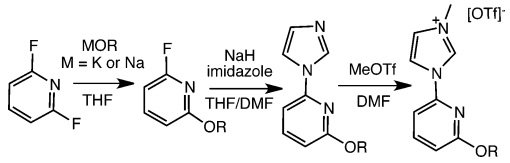

reaction with sodium imidazolate replaced the remaining fluoride to yield 2-alkoxy-6-(*N*-imidazolyl)pyridines (Im-py^{OR}). Alkylation with methyl triflate generated the imidazolium precursors to the NHC ligands (Im^{Me}-py^{OR})OTf.

The carbene ligand was conveniently formed by deprotonation of the imidazolium salt precursor. This deprotonation is readily achieved with mild base, and the acidity of the C-2 proton is evident by observing H/D exchange in the ^{1}H NMR spectra in deuterated protic solvent. Silver bis(carbene) complexes (**6** and **7**) were formed quantitatively through reaction of the imidazolium salts with Ag_2O and NaOH (Scheme 2) (see Chart 2 for our numbering scheme).[45] The

Scheme 2. Synthesis of NHC-py^{OR} Metal Complexes 1−3, 6, and 7

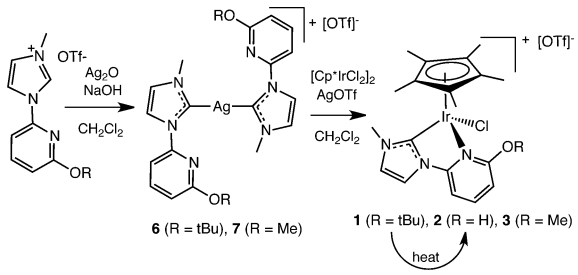

crystal structures of [Ag(NHC-py^{OtBu})$_2$]OTf (**6**) and [Ag(NHC-py^{OMe})$_2$]OTf (**7**) (Figure 1) show that the two NHC-py^{OR} ligands are monodentate with the pyridinol nitrogen atoms not coordinated. The silver ions are two-coordinate with two carbene ligands arranged with approximately linear C−Ag−C angles (172−174°). Interestingly, in the crystal phase, the orientation of the unbound pyridines of the two ligands differs in the two structures. For **6**, the pyridine rings orient to one side of the Ag, and the bulky ^{t}Bu groups are both above the

DOI: 10.1021/acs.organomet.6b00806
Organometallics 2017, 36, 1091−1106

Chart 2. Numbering Scheme for the Compounds Herein[a]

Compound	Formula
1	[Cp*IrCl(NHC-py^{OtBu})]OTf
2	[Cp*IrCl(NHC-py^{OH})]OTf
3	[Cp*IrCl(NHC-py^{OMe})]OTf
4$_{Ir}$	[Cp*IrCl(6,6'-dhbp)]OTf
5$_{Ir}$	[Cp*IrCl(6,6'-dmbp)]OTf
4$_{Ru}$	[(*p*-cymene)RuCl(6,6'-dhbp)]OTf
5$_{Ru}$	[(*p*-cymene)RuCl(6,6'-dmbp)]OTf
6	[Ag(NHC-py^{OtBu})$_2$]OTf
7	[Ag(NHC-py^{OMe})$_2$]OTf

[a]Note that ′ designates the corresponding metal-aqua complex; e.g., **3′** = [Cp*Ir(OH$_2$)(NHC-py^{OMe})]$^{2+}$ as formed in solution by adding AgOTf to **3**.

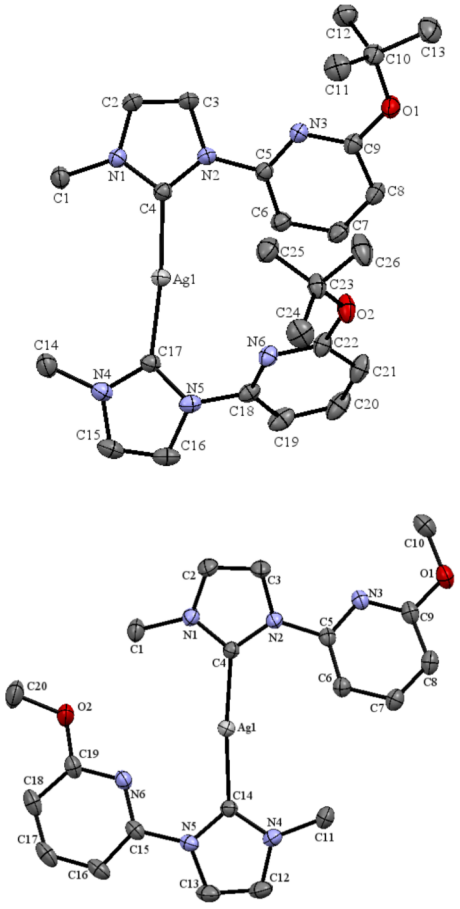

Figure 1. ORTEP diagrams of cations of **6** (top) and **7** (bottom) with hydrogen atoms and counteranions omitted for clarity. Structural parameters are included in the Supporting Information.

general plane of the NHC and Py rings. The packing of these complexes is dominated by the accommodation of the bulky ^{t}Bu groups. For **7**, the methoxy-substituted pyridinol rings are oriented away from each other with out-of-plane rotation of the bond between the NHC and Py rings observed such that one pyridine is pointed in toward the Ag and one is pointed away from the Ag. With little steric hindrance, the crystal packing of these complexes is predominantly due to π-stacking between NHC moieties.

Transmetalation of the silver bis(carbene) complexes **6** and **7** with the iridium dimer [Cp*IrCl$_2$]$_2$ and one equivalent of AgOTf afforded the chelate complexes [Cp*IrCl(NHC^{Me}-py^{OR})]OTf complexes **1** and **3** with R = ^{t}Bu and Me, respectively. The hydroxyl derivative (NHC-py^{OH} in **2**) was synthesized by deprotection of complex **1** via superheating a CH_2Cl_2 solution or reflux of a MeCN solution. Similar to the synthesis of **1** and **3**, the complex [Cp*IrCl(6,6′-dmbp)]OTf (**5$_{Ir}$**) was obtained by adding two equivalents of free 6,6′-dmbp ligand and AgOTf to one equivalent of [Cp*IrCl$_2$]$_2$. All of these complexes are yellow and readily recrystallize by evaporation of acetonitrile or by diffusion with diethyl ether. The crystal structures of these complexes are shown in Figure 2 for **1** and **2** and Figure 3 for **3** and **5$_{Ir}$**.

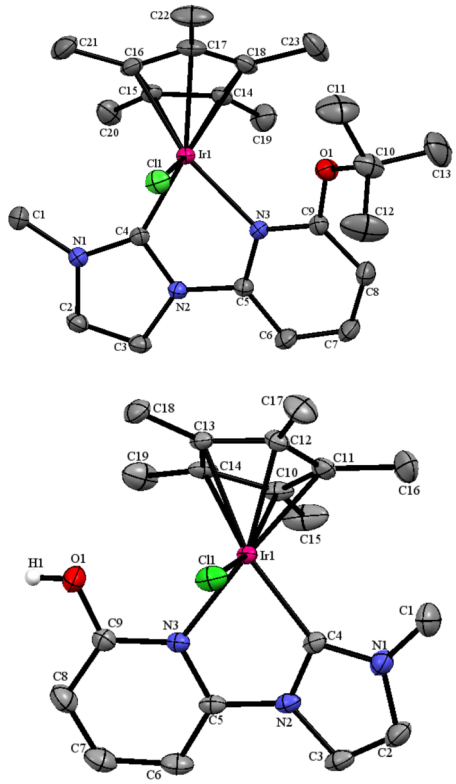

Figure 2. ORTEP diagrams of the cations of **1** (top) and **2** (bottom) with hydrogen atoms and counteranions omitted for clarity. These structures are oriented such that the chloride is forward from the plane of the NHC-py^{OR} ligand. Structural parameters are included in the Supporting Information.

Complexes **2**, **3**, and **5$_{Ir}$** identically pack in the $P2_1/c$ space group such that the chloride of one cation orients above the Cp* ring of an adjacent cation forming chains along the *a* axis with similar distances of 3.438, 3.678, and 3.646 Å, respectively, from Cl1 to the centroid of Cp*. With the bulky *tert*-butyl group, complex **1** packs in the *P*-1 space group. The 6,6′-dmbp complex, [(*p*-cym)RuCl(6,6′-dmbp)]Cl (**5$_{Ru}$**), was synthesized previously by us,[1] but the single-crystal structure was obtained for this paper and belongs to space group $P2_1/n$. Selected dimensions are included in Table 1 for **1**−**3**, **5$_{Ir}$**, and **5$_{Ru}$** and previously reported complexes [Cp*IrCl(6,6′-dhbp)]Cl (**4$_{Ir}$**) and [(*p*-cym)RuCl(6,6′-dhbp)]Cl (**4$_{Ru}$**).[1,2] These complexes all display similar coordination geometries, bond lengths, and angles.

Complex **2** displays a strong, linear hydrogen bond between the OH group and the O- of the triflate counterion (O1 to O4 = 2.638(3) Å, O1−H1−O4 = 173(4)°). Similarly, hydrogen bonding interactions that range from strong to weak have been observed in 6,6′-dhbp complexes of Cu(II),[4,46] Ru(II),[1] and

DOI: 10.1021/acs.organomet.6b00806
Organometallics 2017, 36, 1091−1106

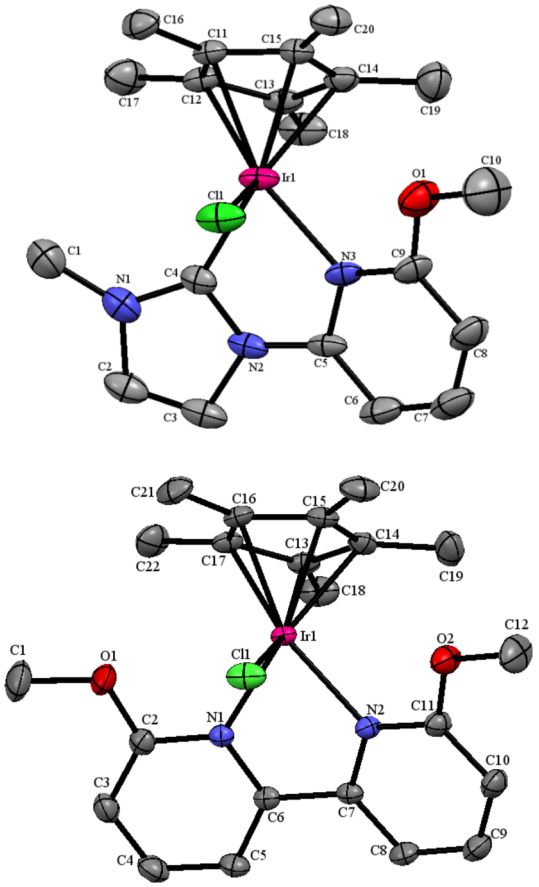

Figure 3. ORTEP diagrams of the cations **3** (top) and $\mathbf{5}_{Ir}$ (bottom) with hydrogen atoms and counteranions omitted for clarity. These structures are oriented such that the chloride is forward from the plane of the bidentate ligand. Structural parameters are included in the Supporting Information.

Ir(III).[2] Inspecting the C−N and C−O distances near the OH/OR group shows that these values are similar in the NHC-py^{OH} and NHC-py^{OtBu} ligands of **1** and **2** as well as in 6,6′-dhbp and 6,6′-dmbp complexes ($\mathbf{4}_{Ir}$ and $\mathbf{5}_{Ir}$ and others in the literature that are not deprotonated).

The bite angle of the two bidentate ligand types, NHC-py^{OR} and dmbp, is nearly identical where the bite angles are within the range of 75−76° for the N−Ir−C or N−Ir−N angles, respectively. It is not surprising that the bite angle is retained for the two types of ligands because both form five-membered chelate rings, and the coordination environments around Ir(III) are similar. Contrary to what is expected from the van der Waal radii of the donor atoms (N < C), the Ir−C distances are slightly shorter than the Ir−N distances (Ir−N_{avg} = 2.10(1) Å and Ir−C_{avg} = 2.04(1) Å for **1**−**3**). This can be rationalized in terms of the strong σ bond donor character of the carbene, and also, Ir to C back bonding is frequently present in NHC complexes.[32] One would expect the Ir−N distance to increase as the bulk of the OR group increases, and this is true for OMe and O^{t}Bu species **3** and **1** [Ir−N 2.07(1) and 2.144(1), respectively]. Note that, to compensate, the Ir−C distance adjusts so that the sum of the Ir−N and Ir−C distances remains constant.[47] OH species **2** shows Ir−N and Ir−C distances between the other two, perhaps because of hydrogen bonding of triflate to the OH, yet the sum of the Ir−N and Ir−C distances remains equal to those of **1** and **3**.

Characterization of complexes **1**−**3** by ^{1}H NMR spectroscopy displays the shielding effect on the protons of the pyridine ring with removal of the protecting group from the ligand NHC-py^{OR} to form the hydroxy group (Figure S45). All of the protons of the pyridine ring are shifted upfield by 0.1−0.2 ppm for complex **2** compared to those of complex **1** with the hydroxy protected by ^{t}Bu and by 0.05−0.15 ppm comparing complex **2** to **3** (hydroxy vs methoxy).

Complex **2** is protic and has a pK_a value of 4.9(1), which is similar to the values of 4.6 and 5 previously measured for $\mathbf{4}_{Ir}$ and $\mathbf{4}_{Ru}$ with the diprotic 6,6′-dhbp ligand bound to Ir(III) and Ru(II), respectively (Table 2).[1,2] As is typically seen, complexation to the metal lowers the pK_a value by several units (6,6′-dhbp has a pK_a value of ∼8.5).[48] The yellow Ir(III) complexes **2** and $\mathbf{4}_{Ir}$ have similar absorption features in the UV−visible spectrum, as seen in Figure 4, with the majority of absorption occurring in the UV region by π to π^* transitions of the aromatic groups of the ligands and weaker charge transfer (CT) and d-d transitions between 300 and 400 nm. The

Table 2. Thermodynamic Acidity (pK_a) Values for the Protic Metal Complexes (2, $\mathbf{4}_{Ru}$, $\mathbf{4}_{Ir}$) Studied Herein and the Free Ligand 6,6′-dhbp

compound	pK_a	ref
2	4.9(1)	this work
$\mathbf{4}_{Ir}$	4.6(1)	2
$\mathbf{4}_{Ru}$	5	1
6,6′-dhbp	8.5	48

Table 1. Selected Bond Lengths and Angles of the Complexes [Cp*IrCl(NHC-py^{OR})]OTf (1−3), [Cp*IrCl(6,6′-dxbp)]$^+$ ($\mathbf{4}_{Ir}$, $\mathbf{5}_{Ir}$), and [(*p*-cym)RuCl(dxbp)]$^+$ ($\mathbf{4}_{Ru}$, $\mathbf{5}_{Ru}$)

		bond lengths (Å)			
compound	bite angle (deg)[a]	Ir1−Cl1	Ir1−N3	Ir1−C4	Ir1−N1 or N2
1	76.00(5)	2.416(4)	2.144(1)	1.997(2)	
2	75.82(9)	2.4143(7)	2.116(2)	2.014(2)	
3[b]	76.1(6) *75(1)*	2.389(7) *2.43(1)*	2.07(1) *2.07(2)*	2.06(2) *2.09(3)*	
$\mathbf{4}_{Ir}$[c]	75.92(8)	2.415(7)			2.10 (2)
$\mathbf{5}_{Ir}$	75.71(6)	2.399(5)			2.117(2) 2.108(1)
		Ru1−Cl1	Ru1−N3	Ru1−C4	Ru1−N1 or N2
$\mathbf{4}_{Ru}$[c]	76.52(5)	2.3899(4)			2.125(1) 2.116(1)
$\mathbf{5}_{Ru}$	76.22(9)	2.3925(9)			2.123(2)2.119(2)

[a]For the bidentate ligand: C, N or N, N. [b]Positional disorder in the bidentate ligand (NHC^{Me}-py^{OMe}) for **3** leads to two sets of metrical parameters. The second set is shown in italics. [c]These crystal structures (for $\mathbf{4}_{Ir}$ and $\mathbf{4}_{Ru}$) were previously reported.[1,2]

DOI: 10.1021/acs.organomet.6b00806
Organometallics 2017, 36, 1091−1106

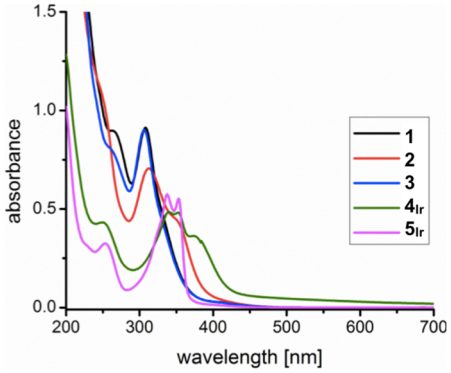

Figure 4. Aqueous UV/visible absorption spectra of the yellow complexes **1**−**3**, $\mathbf{4}_{Ir}$, and $\mathbf{5}_{Ir}$ showing absorption primarily in the UV region.

electronic states of complexes **1** and **3** are shown to be nearly identical by UV−vis, whereas deprotection of the O^{t}Bu to give OH in complex **2** introduces a second CT absorption feature at ∼355 nm comparable to the CT absorption features observed for complex $\mathbf{4}_{Ir}$. There is little change in the absorption features of the halide bound complex **3** vs the aqua bound complex **3′** (Figure S50), suggesting that the Ir(NHC-py^{OR}) complexes have similar electronic properties regardless of whether a halide or aqua ligand fills the coordination sphere.

The similarity of the electronic states of these complexes is again found through the electrochemical investigation of nonaqueous solutions by cyclic voltammetry (Figures S46−S49). For all of the complexes, **1**, **2**, **3**, $\mathbf{4}_{Ir}$, and $\mathbf{5}_{Ir}$, an initial irreversible reduction event is observed below −1 V (all values are reported vs SCE) forming some complex that has a return oxidation event at a more positive potential, which is only observed if the initial complex first undergoes the irreversible reduction event. Aprotic complexes **1** and **3** have nearly identical irreversible reduction events at approximately −1.60 V; upon scanning to more positive potentials, new irreversible oxidation events at −0.90 V in MeCN were seen (Figure S46). Complex $\mathbf{5}_{Ir}$ with a 6,6′-dmbp ligand exhibits similar behavior with initial reduction at −1.25 V and, on return to more positive potential, a new oxidation at −0.83 V (Figure S47). However, when the OR group of the pyridine is deprotected to form the protic hydroxyl group, as in the case of complexes **2** and $\mathbf{4}_{Ir}$, the return oxidation events occur at a much larger difference in potential than for the complexes in which the hydroxyl group is protected. Because of the lower solubility of complex $\mathbf{4}_{Ir}$, the CV was performed in DMF (Figure S48). The initial irreversible reduction event occurred at −1.60 V in MeCN and −1.55 V in DMF for complex **2** and at −1.40 V in DMF for complex $\mathbf{4}_{Ir}$, whereas the return oxidation events occur at 0.36, 0.33, and 0.95 V, respectively. The corresponding Δ_p between the irreversible reduction and oxidation events are 1.96 V in MeCN, 1.88 V in DMF for complex **2**, and 2.35 V for complex $\mathbf{4}_{Ir}$. Recently, Re complexes with aprotic NHC-py ligands have been reported, which similarly show a large difference in the initial irreversible reduction event followed by a "delayed" irreversible oxidation event; the reduction was ascribed to pyridyl ligand forming a radical anion (Py$^{\cdot-}$).[38] In the case of both complex **2** and $\mathbf{4}_{Ir}$, the addition of base forced reduction to occur at more negative potentials, as could be expected from formation of an alkoxide substituent and diminished the current of the return irreversible oxidation event (Figure S49).

Catalytic CO_2 Hydrogenation: Enhancing Activity. The new NHC-py^{OR} complexes along with bipy complexes were tested for the catalysis of the hydrogenation of CO_2 to formate (Table 3). Here, we only report the TON value after 18 h for

Table 3. Catalytic Hydrogenation of CO_2 with 1−5[a]

		catalyst used as is		Cl$^-$ removed in situ	
entry	catalyst	TON	TOF (h^{-1})	TON	TOF (h^{-1})
1	$[Cp^*IrCl_2]_2$	180 (20)	10		
2	**1**	1090 (20)	60.6	740 (30)	41
3	**2**	910 (60)	51	860 (100)	48
4	**3**	2020 (90)	112	2090 (60)	116
5	$\mathbf{4}_{Ir}$	2270 (90)	126	2400 (70)	130
6	$\mathbf{5}_{Ir}$	410 (220)[b]	29	290 (60)	16
7	$\mathbf{4}_{Ru}$	1070 (20)	59.4	2270 (100)	126
8	$\mathbf{5}_{Ru}$	890 (330)[b]	49	1220 (30)	67.8

[a]Conditions: The reactions were performed in 25 mL of an aqueous solution of 0.3 mM catalyst and 1 M $NaHCO_3$ at 115 °C and 300 psig of H_2/CO_2 (1:1). All TON are calculated after 18 h and are an average of at least 3 experiments (estimated standard deviations are in parentheses). TOF values are for the full 18 h period (TOF = TON/18 h). Data are reported to at most three significant figures based on the measurements. Entries 3, 5, and 7 are performed with OH-containing catalysts (**2** with NHC-py^{OH} and $\mathbf{4}_{Ir}$ and $\mathbf{4}_{Ru}$ with 6,6′-dhbp). The other entries used alkoxy-substituted catalysts (**1** with NHC-py^{OtBu}, **3** with NHC-py^{OMe}, and $\mathbf{5}_{Ir}$ and $\mathbf{5}_{Ru}$ with 6,6′-dmbp). [b]Gave highly variable TON; may be forming nanoparticles.

catalysts **1**−**5**, but in the SI, we report the pressure drop as a function of time for these catalysts (Figures S59−79). The rate of pressure drop is approximately constant over the course of the 18 h for all of these catalysts (Figure S80). A control reaction was performed with $[Cp^*IrCl_2]_2$ (0.15 mM of dimer or 0.30 mM in iridium) tested as a catalyst, and this produced 0.686 mmol of formate corresponding to 180 TON (entry 1, Table 3). Hence, $[Cp^*IrCl_2]_2$ is 11.2−12.6 times less active than the most active catalysts tested (**3** and $\mathbf{4}_{Ir}$), implicating a significant role of the organic ligands. No other CO_2 reduction products besides formate were observed in these reactions.

For the new NHC-py^{OR} derivatives, the order of activity is **3** > **1** ≈ **2**, with **3** being almost twice as active as either **1** or **2**. Compounds **1**−**3** are best considered to be precatalysts as they all undergo significant transformations in solution (see below).

The trend is different with complexes of the dxbp-type ligands. The hydroxy dxbp complexes ($\mathbf{4}_{Ir}$ or $\mathbf{4}_{Ru}$) are more active than the methoxy complexes ($\mathbf{5}_{Ir}$ or $\mathbf{5}_{Ru}$). These hydrogenation experiments were run in 1 M $NaHCO_3$, under basic conditions (pH 8.5), where the hydroxy groups are deprotonated to give the more electron-donating oxyanions that are proposed to enhance catalysis.[49] Comparing metals in literature examples, iridium complexes are generally more active than ruthenium complexes, and this trend holds true here for dhbp complexes ($\mathbf{4}_{Ir}$ > $\mathbf{4}_{Ru}$) but not for the dmbp analogues ($\mathbf{5}_{Ir}$ < $\mathbf{5}_{Ru}$). However, the results for both $\mathbf{5}_{Ir}$ and $\mathbf{5}_{Ru}$ were inconsistent and suggest catalyst modification (further discussed in the SI).

Comparing monodentate ligands (chloride, triflate, water) at the catalyst active site, it has been shown that the presence of halide can poison a (de)hydrogenation catalyst, presumably by favorable binding to the active site.[17] Therefore, we removed the chloride by adding silver triflate to the catalyst solution; the precipitated silver chloride was easily removed by filtration. The

DOI: 10.1021/acs.organomet.6b00806
Organometallics 2017, 36, 1091−1106

filtrate was then used directly for catalysis without isolation (in situ halide removal in Table 3). For precatalysts **1**–**3**, the removal of the chloride does not increase the catalytic activity; silver-triflate-treated **1** and **2** even decrease slightly in activity. However, when treated, $\mathbf{4}_{Ru}$ (with 6,6′-dhbp bound to Ru) shows a large increase in activity, which more than doubles with the removal of the chlorides (to 95% of the activity of $\mathbf{4}_{Ir}$, the Ir analogue). Notably, ruthenium is 10 times cheaper than iridium, and although Ru complex $\mathbf{4}_{Ru}$ was reported in 2011,[1] it had not previously been used for CO_2 hydrogenation.

The base used in CO_2 hydrogenation, $NaHCO_3$, provides a Lewis acid (Na^+) that can potentially impact the rate of the reaction. To test this hypothesis, we varied the base and used $KHCO_3$, $CsHCO_3$, and $(NH_4)HCO_3$, which were chosen as commercially available bicarbonate salts (Table 4). The K^+ and

Table 4. Effect of the Lewis Acid on CO_2 Hydrogenation with $\mathbf{4}_{Ir}$[a]

entry	M^+	pH	TON
1	Na^+	8.1 (1)	1430 (70)
2	K^+	8.3 (1)	1410 (50)
3	Cs^+	8.4 (1)	1390 (50)
4	NH_4^+	7.8 (1)	500 (80)

[a]Conditions: The reactions were performed in 25 mL of an aqueous solution of 0.3 mM catalyst and 0.5 M $MHCO_3$ (M = Na, K, Cs, or NH_4) at 115 °C and 300 psig of H_2/CO_2 (1:1). All TON are calculated after 18 h and are an average of at least 3 experiments (estimated standard deviations are in parentheses).

Cs^+ salts give similar or higher pH values for the resulting solution (see third column of Table 4), but the pH does drop slightly with the NH_4^+ salt (pH 7.8). The Na, K, and Cs bicarbonate salts all gave similar TON values with $\mathbf{4}_{Ir}$, whereas the ammonium bicarbonate salt gave a significantly lower TON. Similarly, when we monitor the pressure over time (Figures S81–S84), the rate of pressure drop is similar to that of the alkali metals over the entire course of the reaction; it is much slower with NH_4^+. In Table 4, the almost 3-fold greater TON seen in entries 1–3 than in entry 4 is a fact whose mechanistic implications will be discussed in the section below on computations.

Catalytic CO_2 Hydrogenation: Precatalyst Transformations. Interestingly, UV–vis absorption spectroscopy of complex $\mathbf{4}_{Ir}$ shows that the catalyst remained mostly unchanged after hydrogenation, yet for $\mathbf{5}_{Ir}$, significant bleaching of the CT features was observed (Figure S52). In short, the robust nature of $\mathbf{4}_{Ir}$ as compared to $\mathbf{5}_{Ir}$ is a main factor for the higher TON observed in Table 3. Significant color changes were observed visually for NHC-py^{OR} complexes **1**–**3** after hydrogenation, which was quantitated by measuring UV–vis absorption (Figure S51). The CT absorption features for the starting complexes bleached, leaving significant absorption only in the UV range.

We were able to elucidate transformations of complex **3** (full details, SI pp. S34–43). ^{1}H NMR spectral evidence after hydrogenation (Figure S53) shows that some **3** remains, but some has been converted to cyclometalated product **3″** as shown in Scheme 3. Complex **3″** is formed by treating **3** with our hydrogenation conditions or by heating **3** in an inert solvent with base (e.g., treating **3** with Na_2CO_3 in CH_2Cl_2).

Although we were unable to recrystallize **3″**, we did trap a cyclometalated species by treating **3** with triethylamine in

Scheme 3. (top) Formation of Cyclometalated 3″ and Further Products under Hydrogenation Conditions; (bottom) Product 3_{SP} Results when 3 is Treated with Dichloroethane and Base

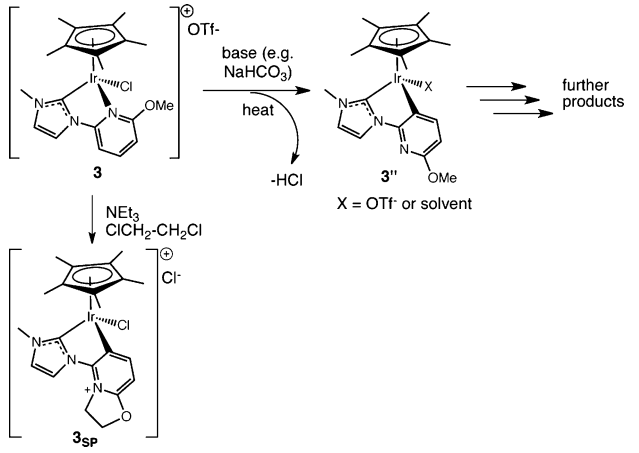

dichloroethane. The resulting product $\mathbf{3}_{SP}$ was isolated in 48% yield, as characterized by ^{1}H NMR and MS methods (Figures S54–55), and recrystallized by slow diffusion of ether into acetonitrile. A crystal structure is shown in Figure S91. As shown in Scheme 3, the product $\mathbf{3}_{SP}$ appears to result from an S_N2 reaction between **3″** and dichloroethane along with surprising loss of the methyl group from the methoxy substituent. In $\mathbf{3}_{SP}$, the bidentate CC ligand (bite angle = 77.4(3)°) is best described as a zwitterion with a cationic N and an anionic C of the C-bound pyridyl ligand. The metal is still Ir(III), and the complex is cationic. The metrical parameters including Ir–C(NHC) = 1.996(5) Å and Ir–C(Py) = 2.054(7) Å are similar to those in Table 1 and analogous Ir(III) complexes in the literature.[21] Although $\mathbf{3}_{SP}$ is not the same as the cyclometalated product **3″** obtained under hydrogenation conditions, the pattern of signals in ^{1}H NMR spectra of **3″** and $\mathbf{3}_{SP}$ does confirm that the transformation of **3** involves cyclometalation of the pyridine ring.

There is precedent in the literature for cyclometalation of bidentate NHC-pyridine ligands on iridium[37] and rhodium.[51] Cyclometalation has also been reported for 6,6′-dmbp complexes of gold, palladium, and platinum,[51,52] but we have not observed cyclometalation of the dxbp complexes herein.

After 18 h under basic CO_2 hydrogenation conditions, **3** is converted to a blue solid mixture that appears to contain **3″** (see Figure S53) and new, unidentified products. The elemental makeup of this water-soluble blue solid is described in the SI from XPS and EDS data (Figures S56–S58); reduced C and loss of Cl, F, and S but retention of Ir, N, and O suggest that perhaps Cp* loss occurs from **3″** after cyclometalation.[50]

Formic Acid Dehydrogenation. Dehydrogenation of formic acid was performed with complexes **1**–**5**. In each trial, 1.02 M formic acid with 0.29 mM catalyst was heated at 60 °C for 3 h (Table 5).

All three iridium complexes of the new NHC-py^{OR} ligands (**1**–**3**) were found to be active precatalysts (entries 1–3). These precatalysts can also be compared to iridium and ruthenium complexes of 6,6′-dhbp and 6,6′-dmbp (entries 4–7), of which the iridium complexes of 6,6′-dxbp are by far the most active. We also note that the estimated standard deviations in TON values are higher for **1**–**3** (as compared with **4** and **5**) and may reflect variables related to the

DOI: 10.1021/acs.organomet.6b00806
Organometallics 2017, 36, 1091–1106

Table 5. Dehydrogenation of Formic Acid by Catalysts 1−5[a]

		catalyst used as is		Cl^- removed in situ	
entry	catalyst	TON	TOF (h^{-1})	TON	TOF (h^{-1})
1	**1**	130 (30)	44	200 (40)	66
2	**2**	90 (50)	31	140 (30)	47
3	**3**	180 (60)	59	80 (20)	27
4	$\mathbf{4}_{Ir}$	>3500[b]	1200	>3500[b]	1200
5	$\mathbf{5}_{Ir}$	>3500[b]	1200	>3500[b]	1200
6	$\mathbf{4}_{Ru}$	45 (12)	15	46 (6)	15
7	$\mathbf{5}_{Ru}$	140 (10)	45	16 (2)	5

[a]Conditions: Aqueous formic acid (1.02 M) was treated with catalysts **1**−**5** (0.29 mM) at 60 °C for 3 h. In the right two columns, chloride was removed by treating with silver salts in situ. See the Experimental Section for further details. Turnover numbers (TON) and turnover frequency (TOF) values were calculated to two significant figures at the end of the 3 h period by measuring the gas generated (assuming 1:1 of CO_2/H_2). TON values are an average of at least 3 experiments (estimated standard deviations are in parentheses). Entries 2, 4 and 6 were performed with OH-containing catalysts (**2** with NHC-py^{OH} and $\mathbf{4}_{Ir}$ and $\mathbf{4}_{Ru}$ with 6,6′-dhbp). The other entries used alkoxy-substituted catalysts (**1** with NHC-py^{OtBu}, **3** with NHC-py^{OMe}, and $\mathbf{5}_{Ir}$ and $\mathbf{5}_{Ru}$ with 6,6′-dmbp). [b]These experiments went to 99.8−100% conversion of formic acid to gaseous products; in addition to measuring gas formation, we also double checked these values by ^{1}H NMR spectroscopic analysis of an aliquot of the solution phase, and these reactions only leave 0−0.2% of formic acid unconsumed.

transformation of the NHC-py^{OR} complexes **1**−**3** (see the SI for further details). Because complexes **4** and **5** appear to be robust catalysts, we focus on them here.

Notably, when we replace 6,6′-dhbp with 6,6′-dmbp in [Cp*Ir(6,6′-dmbp)Cl]OTf ($\mathbf{5}_{Ir}$), we see that the catalyst has comparable activity (entry 5). Significantly, the literature on $\mathbf{4}_{Ir}$ describes how hydroxy groups are needed for a metal−ligand bifunctional mechanism,[9] but the similar reactivity of $\mathbf{5}_{Ir}$ and $\mathbf{4}_{Ir}$ suggests that other effects are at work. Our groups provided evidence from X-ray crystallography and reactivity studies of the dmbp complex [(terpy)Ru(6,6′-dmbp)(H_2O)]$(OTf)_2$ that the methoxy group can accept a hydrogen bond from the coordinated aquo ligand,[3] and thus, hydrogen bond acceptance by the oxygenated substituents of $\mathbf{5}_{Ir}$ and $\mathbf{4}_{Ir}$ during catalysis may play a role. Formic acid dehydrogenation is performed under acidic conditions (pH 1.9); hence, none of the OH groups are deprotonated (pK_a = 4.6 and 5 for $\mathbf{4}_{Ir}$ and $\mathbf{4}_{Ru}$, respectively)[1,2] and may behave similar to methoxy groups as hydrogen bond acceptors and electron-donating groups. Upon replacing the iridium with ruthenium in $\mathbf{4}_{Ru}$ (with 6,6′-dhbp) and $\mathbf{5}_{Ru}$ (with 6,6′-dmbp), we see that the resulting catalysts are far less active (entries 6 and 7).

The shaded cells in Table 5 show the reactivity of OH-substituted catalysts from which it is readily apparent (entries 2 and 4) that 6,6′-dhbp-ligated catalysts are far more active than the complexes of the NHC-py^{OH} ligand. The lesser reactivity may be caused by transformation(s) of the NHC-py^{OR}-ligated complexes.

The catalyst [Cp*IrCl(6,6′-dmbp)]OTf ($\mathbf{5}_{Ir}$) was further studied over a longer time course as a highly active species of novel structure. Table S22 shows the longevity of $\mathbf{5}_{Ir}$ by adding substrate (formic acid) after each reaction cycle was complete (every 3 h). UV−vis absorption spectra of the catalytic mixtures before and after dehydrogenation show that the complexes are unaltered (Figure S87). Complete conversion of formic acid to gaseous products occurs quantitatively (~100% yield) for five

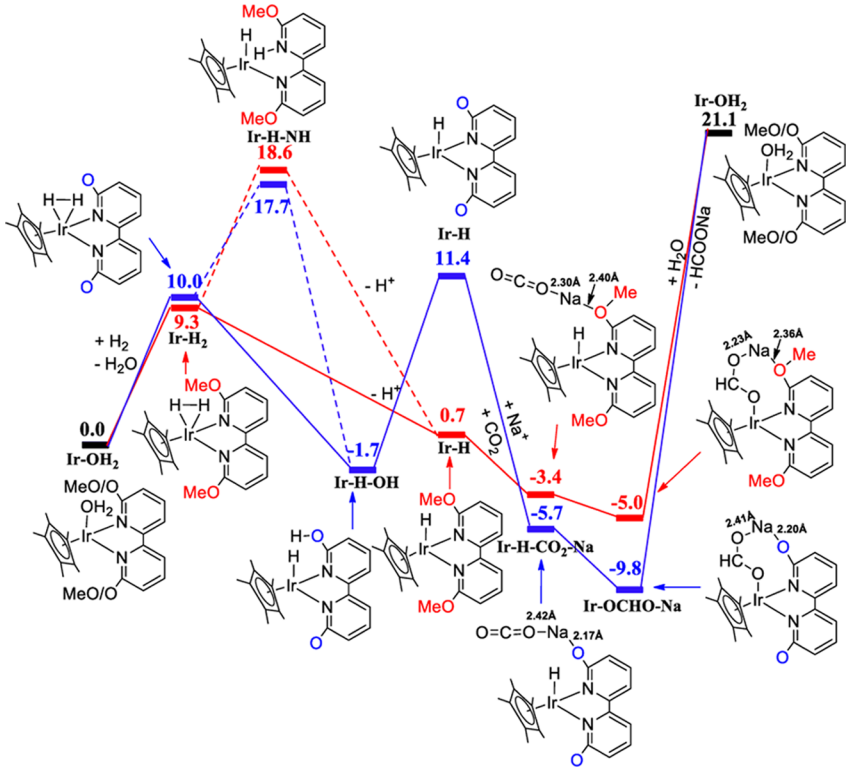

Figure 5. Diagram of minima with relative energies (solvent corrected energies in kcal/mol) of CO_2 hydrogenation catalyzed by $\mathbf{4}_{Ir}$ and $\mathbf{5}_{Ir}$ with the assistance of Na^+ ion. The blue bars with the blue solid line represent the pathway of $\mathbf{4}_{Ir}$, and the red bars with the red solid line represent the pathway of $\mathbf{5}_{Ir}$. The dashed line represents the pathway via the Ir-hydride with protonated pyridine species.

DOI: 10.1021/acs.organomet.6b00806
Organometallics 2017, 36, 1091−1106

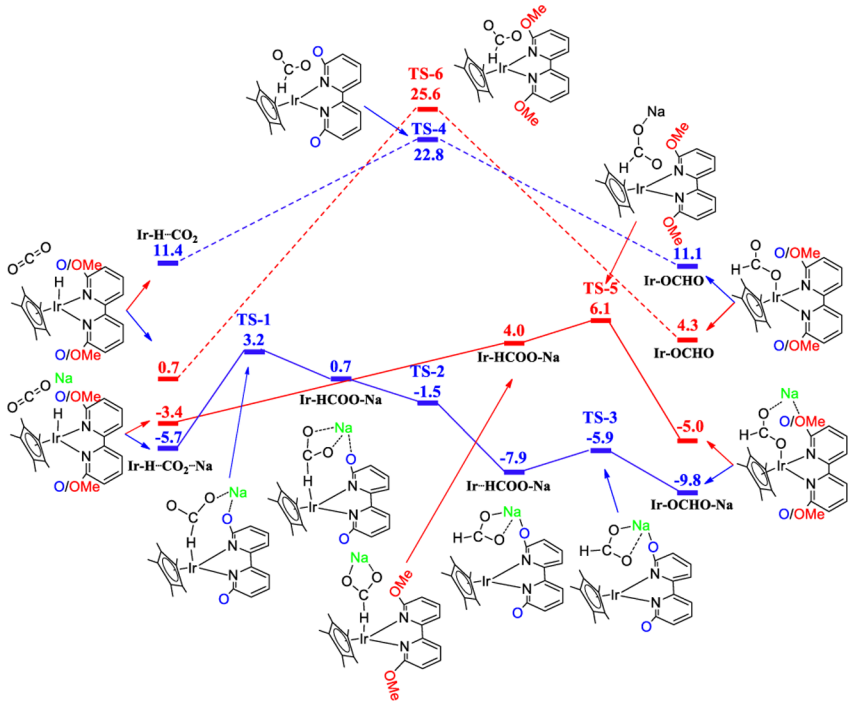

Figure 6. Free energy diagram (solvent corrected energies in kcal/mol) of CO_2 insertion into the iridium hydride of $\mathbf{4}_{Ir}$ and $\mathbf{5}_{Ir}$ with and without the assistance of a Na^+ ion. The blue bars with the solid line represents the pathway of $\mathbf{4}_{Ir}$, and red bars with the solid line represent the pathway of $\mathbf{5}_{Ir}$. The dashed line represents the pathways without the assistance of the Na^+ ion.

cycles run over 3 d. Only after gentle heating at 60 °C for 3 d without added substrate does catalyst deactivation occur. Thereafter, when formic acid is added, a decrease in TOF was observed. A maximal TON of 21,000 was observed at this point (after 8 d), but the ultimate value would be higher because the catalyst is still active. A ^1H NMR spectrum acquired after concentrating the same reaction mixture shows that the major component is still the original catalyst (Figure S88).

A lower loading of catalyst $\mathbf{5}_{Ir}$ (0.0028 mol % catalyst or 10 times lower relative to the conditions of Table 5) was also investigated (Table S23). Here, the TOF is ~2.8 times faster at ~3300 h^{-1} with only 29% conversion at 3 h. For comparison, the TOF values over 3 h are ~1200 h^{-1} at 0.028 mol % of $\mathbf{5}_{Ir}$. A 10-fold increase in turnover frequency was anticipated with dropping the catalyst loading, but it appears that at the low catalyst loading the reaction occurs more slowly due to the saturation of all the catalyst sites or that catalyst decomposition interferes. At 0.0028 mol % of catalyst $\mathbf{5}_{Ir}$ loading, the reaction does go to 94% conversion (TON = 33,000) after 24 h; thus, if given enough time, the yield of product is nearly quantitative even at very low catalyst loadings.

Computational Study of Catalytic CO_2 Hydrogenation. Hydrogenation reactions described herein using 6,6′-dhbp are proposed to proceed via a metal−ligand bifunctional mechanism. We expect that the OH/O- groups will play a role in transferring protons. This mechanism will be illustrated using $\mathbf{4}_{Ir}$, which was the most active catalyst for hydrogenation. We will compare $\mathbf{4}_{Ir}$ computationally with $\mathbf{5}_{Ir}$, the 6,6′-dmbp complex, which was considerably less active. The anionic oxygen of the deprotonated 6,6′-dhbp ligand can bind Na^+ to activate CO_2 and hold substrate near the metal center. Interactions between alkali metals and substrates have literature precedent, and the identity of the alkali metal can greatly impact the rates.[53−58] We note that most of the studies on the role of alkali metals have been in alcoholic solvents, and ours is the first to use water. Although $[Cp^*Ir(OH_2)(6,6'\text{-dhbp})]^{2+}$, $\mathbf{4}_{Ir}'$, has been computationally studied for CO_2 hydrogenation,[59] our mechanism is unique in describing the role of the alkali metal and in contrasting dxbp complexes $\mathbf{4}_{Ir}$ and $\mathbf{5}_{Ir}$. Under our typical hydrogenation conditions (Table 3), $[Na^+]$ = 1 M and $[H^+] = 3.2 \times 10^{-9}$ M at pH 8.5. Thus, we invoke the use of Na^+ rather than H^+ (as used by Ertem et al.[59]) under basic conditions.

The proposed mechanisms of CO_2 hydrogenation catalyzed by $\mathbf{4}_{Ir}$ and $\mathbf{5}_{Ir}$ with and without the assistance of Na^+ ion are shown in Figure 5 and Figure S85, respectively. Hydrogenation reactions were run in aqueous base (pH 8.5), and thus for $\mathbf{4}_{Ir}$, the 6,6′-dhbp ligand will first be deprotonated to form the species with the dianionic ligand (6,6′-bobp, 6,6′-bis-O^--bipyridine). The activation of dihydrogen leads to $\mathbf{Ir-H_2}$, a σ complex, as the first intermediate. The acidic dihydrogen complex can transfer a proton two ways. With $\mathbf{5}_{Ir}$, proton transfer to solvent occurs directly leading to **Ir−H**. With $\mathbf{4}_{Ir}$, the O of the dianionic ligand can be protonated to give the **Ir−H−OH** species before loss of a proton and formation of **Ir−H** (water may assist this process).[59] [The formation of a protonated pyridine species (**Ir−H−NH**) is energetically unfavorable for both $\mathbf{4}_{Ir}$ and $\mathbf{5}_{Ir}$ (17.7 and 18.6 kcal/mol, respectively).] After the formation of **Ir−H**, one CO_2 molecule could be involved with the assistance of Na^+ ion to form the **Ir−H−CO_2** species. The **Ir−H−CO_2-Na** species could then be converted to the Ir-formate species (**Ir-OCHO-Na**), which then would generate the final product $HCOO^-$. The species thus formed would be lower-energy with the Na^+ interacting with the dianionic 6,6′-bobp ligand as compared with the dmbp ligand (for $\mathbf{4}_{Ir}$ and $\mathbf{5}_{Ir}$: **Ir−H−CO_2-Na** at −5.7 and −3.4 kcal/mol and **Ir-OCHO-Na** at −9.8 and −5.0 kcal/mol,

DOI: 10.1021/acs.organomet.6b00806
Organometallics 2017, 36, 1091−1106

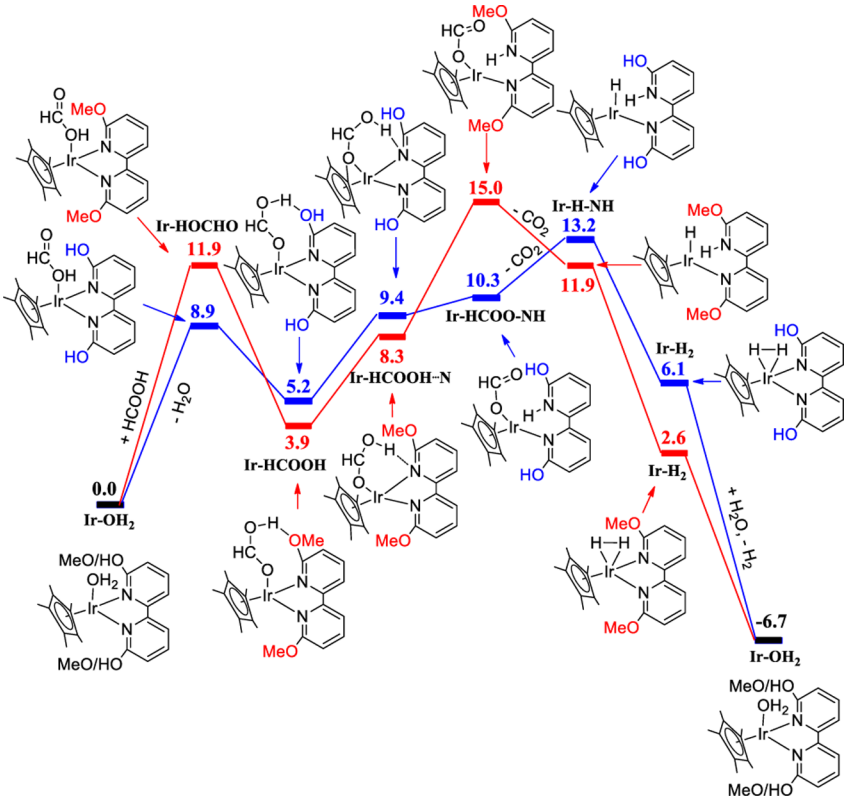

Figure 7. Diagram of minima with relative energies (solvent corrected energies in kcal/mol) of intramolecular proton transfer-involved formic acid dehydrogenation catalyzed by $\mathbf{4}_{Ir}$ and $\mathbf{5}_{Ir}$. The blue bars with the solid line represent the pathway of $\mathbf{4}_{Ir}$, and red bars with the solid line represent the pathway of $\mathbf{5}_{Ir}$.

respectively). The weaker stabilization of Na^+ ion with $\mathbf{5}_{Ir}$ as compared to $\mathbf{4}_{Ir}$ was also confirmed by the longer Na-OMe distances in the **Ir−H−CO$_2$-Na** (2.40 vs 2.17 Å) and **Ir-OCHO-Na** species (2.36 vs 2.20 Å). Thus, $\mathbf{4}_{Ir}$ is predicted to have better catalytic activity than $\mathbf{5}_{Ir}$ in CO_2 hydrogenation with alkali metals present, as is experimentally observed. Without Na^+ ion, a much higher-energy intermediate is observed (**Ir-OCHO** at 18.8 and 12.4 kcal/mol for $\mathbf{4}_{Ir}$ and $\mathbf{5}_{Ir}$, respectively; Figure S85). This shows the importance of the Lewis acid (Na^+) in CO_2 hydrogenation.

The related transition states (proceeding from **Ir−H−CO$_2$** to **Ir-OCHO**) located in Figure 6 verify the importance of Na^+ ion in the CO_2 insertion step of the hydrogenation reaction. The transition state free energies are much higher without the assistance of a sodium ion (22.8 and 25.6 kcal/mol for $\mathbf{4}_{Ir}$ and $\mathbf{5}_{Ir}$, respectively). With the Na^+ ion present, CO_2 insertion into the **Ir−H** of $\mathbf{4}_{Ir}$ was achieved by two lower-energy intermediate Na^+-ion stabilized species (**Ir-HCOO-Na** at 0.7 kcal/mol with a weak Ir−H interaction and **Ir-HCOO-Na** at −7.9 kcal/mol without direct interaction between Ir to H; Figure 6). The turnover-limiting step in the CO_2 insertion process catalyzed by $\mathbf{4}_{Ir}$ with the assistance of Na^+ ion gave a much lower Gibbs free energy compared to that without the assistance of Na^+ ion (3.2 vs 22.8 kcal/mol). Similar results were also observed for the $\mathbf{5}_{Ir}$ (6.1 vs 25.6 kcal/mol). These related transition states during the CO_2 hydrogenation reaction catalyzed by $\mathbf{4}_{Ir}$ and $\mathbf{5}_{Ir}$ show the important role of the Na^+ ion in the stabilization of reaction intermediates and also demonstrate that $\mathbf{4}_{Ir}$ is predicted to have better catalytic activity than $\mathbf{5}_{Ir}$ in CO_2 hydrogenation. (We propose that the use of NH_4^+ would give activation barriers slightly higher than that observed for Na^+ based upon Table 4; we note that ammonium can still donate hydrogen bonds but it is a weaker Lewis acid than Na^+.)

The H_2 cleavage process catalyzed by $\mathbf{4}_{Ir}$ (Figure S86) demonstrates that the pathway from **Ir−H$_2$** σ complex to Ir-hydride with hydroxy group species (**Ir−H−OH**) was more favorable than the pathway from **Ir−H$_2$** σ complex to Ir-hydride with protonated pyridine species (**Ir−H−NH**) (11.0 vs 28.7 kcal/mol). It is worth noting that an Ir-dihydride species (**Ir-2H**) was observed for the H_2 cleavage process catalyzed by $\mathbf{5}_{Ir}$ (Figure S86). The transition state of the conversion between the **Ir−H$_2$** σ complex and **Ir-2H** dihydride species has not yet been located; however, this process will be facile. The free energy of activation for the conversion between **Ir-2H** dihydride and Ir-hydride with protonated pyridine species (**Ir−H−NH**) of $\mathbf{5}_{Ir}$ was much higher than that of $\mathbf{4}_{Ir}$ (33.9 vs 28.7 kcal/mol). Computations of the CO_2 insertion process with the assistance of Na^+ ion and H_2 cleavage process were consistent with the experimental observation that $\mathbf{4}_{Ir}$ has better catalytic activity than that of $\mathbf{5}_{Ir}$ in CO_2 hydrogenation.

In summary, our proposed mechanism invokes a role for the oxyanion of dhbp and explains why the dhbp complexes are more active than the dmbp complexes for CO_2 hydrogenation at basic pH. Remarkably, the important role of the secondary coordination sphere in hydrogenation may help explain why the activity of $\mathbf{4}_{Ru}$ is 95% of that seen with $\mathbf{4}_{Ir}$. In this manner, a less expensive metal (ruthenium) can work nearly as well as iridium when paired with an appropriate ligand.

Computational Study of Formic Acid Dehydrogenation. Recall that OH and OMe groups in dxbp complexes ($\mathbf{4}_{Ir}$ and $\mathbf{5}_{Ir}$) produced similar rates of dehydrogenation. Under acidic conditions (pH 1.9 for dehydrogenation of aqueous

DOI: 10.1021/acs.organomet.6b00806
Organometallics 2017, 36, 1091−1106

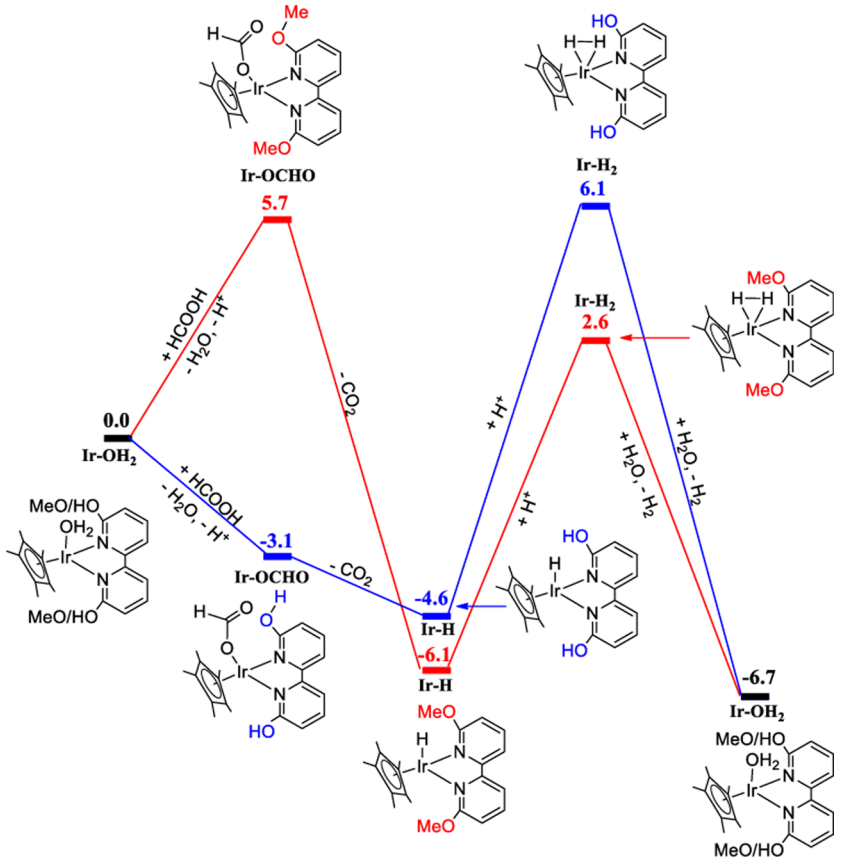

Figure 8. Diagram of minima with relative energies (solvent corrected energies in kcal/mol) of intermolecular proton transfer-involved formic acid dehydrogenation catalyzed by $\mathbf{4}_{Ir}$ and $\mathbf{5}_{Ir}$. The blue bars with the solid line represent the pathway of $\mathbf{4}_{Ir}$, and the red bar with the solid line represent the pathway of $\mathbf{5}_{Ir}$.

formic acid), the OH groups in dhbp will not be deprotonated and will behave similarly to the OMe groups. Again, the dehydrogenation of formic acid has been studied previously with $\mathbf{4}_{Ir}$',[59] but our study is unique in comparing the role of OH vs OMe groups.

The possible mechanisms of formic acid dehydrogenation catalyzed by $\mathbf{4}_{Ir}$ and $\mathbf{5}_{Ir}$ with intramolecular or intermolecular proton transfer (Figures 7 and 8) were also explored. Formic acid can first bind to Ir via the hydroxyl group (**Ir-HOCHO**) under acidic aqueous conditions. Then, a lower energy species is formed by conversion to the species (**Ir-HCOOH**) with formic acid's OH hydrogen bonded species to the OH or OMe of the dxbp ligand. The hydrogen bonds between OH of **Ir-HCOOH** and N of the dxbp and the following intramolecular proton transfer lead to the formation of an Ir-formate species with protonated pyridine (**Ir-HCOO-NH**). Subsequent β-hydride elimination produces CO_2 and the Ir-hydride species with protonated pyridine (**Ir−H−NH**). The iridium hydride can be protonated intramolecularly by the NH to form an η^2-H_2 σ complex (**Ir−H_2**), which finally releases an H_2 molecule. The relatively small differences of the values of reaction energies in the formic acid dehydrogenation process catalyzed by $\mathbf{4}_{Ir}$ and $\mathbf{5}_{Ir}$ with intramolecular proton transfer is consistent with the similar catalytic activities observed. Figure 8 focuses on intermolecular proton transfer, for example, that of HCOOH directly to solvent as it binds to Ir to give the Ir-formate species (**Ir-OCHO**). Here, the dhbp analogue is stabilized relative to the dmbp complex by intramolecular hydrogen bonds. In contrast, subsequent minima in Figure 8 differ by no more than 3.5 kcal mol^{-1} as a function of bipy substituent, consistent with operation of intermolecular proton transfer pathways in the formic acid dehydrogenation process catalyzed by $\mathbf{4}_{Ir}$ and $\mathbf{5}_{Ir}$.

CONCLUSIONS

In summary, we have synthesized a new bidentate ligand with an NHC ring bound to a pyridinol ring. The resulting NHC-py^{OR} complexes of iridium(III) are moderately active precatalysts for the hydrogenation of CO_2. Low activity is observed when these NHC-py^{OR} complexes (**1**−**3**) are used for formic acid dehydrogenation. The NHC-pyridinol-derived ligands appear to undergo a cyclometalation reaction under basic conditions, and we have trapped a cyclometalated product.

In contrast, the 6,6′-dhbp ligands and complexes thereof are more stable and products of further transformations are not observed. The iridium 6,6′-dhbp complexes have been used for CO_2 hydrogenation in the literature,[6,9] and similarly, we observe that these are highly active catalysts for both hydrogenation and dehydrogenation. However, we have extended this work toward ruthenium and 6,6′-dmbp ligands. Our groups and others have described the secondary coordination sphere influence of 6,6′-dhbp and its benefits toward reductive catalysis, specifically, CO_2 reduction.[1,6,9,53,60,61] Not surprisingly, under basic conditions, catalysts for hydrogenation with the diprotic ligand 6,6′-dhbp are 5−8 times more active than catalysts using the aprotic analogue 6,6′-dmbp. Remarkably, ruthenium ($\mathbf{4}_{Ru}$) is nearly (95%) as active as iridium ($\mathbf{4}_{Ir}$) with 6,6′-dhbp, and this can be

DOI: 10.1021/acs.organomet.6b00806
Organometallics 2017, 36, 1091−1106

rationalized in terms of the secondary coordination sphere having a big impact on catalysis despite the difference in metal. Computationally, this assertion is supported by observing how binding Na^+ near the metal (in $\mathbf{4}_{Ir}$) serves to lower the free energy barriers for CO_2 hydrogenation.

However, we see the secondary coordination sphere is not as important for dehydrogenation under acidic conditions. Here, iridium is more active than ruthenium, and methoxy and hydroxy perform similarly (in $\mathbf{5}_{Ir}$ and $\mathbf{4}_{Ir}$, respectively). Thus, the nature of x in dxbp does not matter if the pH is such that the OH groups are not deprotonated. Electronically, OH and OMe groups are similar and both can accept hydrogen bonds.[3] Computationally, we can explain this similarity in terms of similar energy barriers for dehydrogenation of formic acid with $\mathbf{4}_{Ir}$ and $\mathbf{5}_{Ir}$.

In summary, we have determined how subtle ligand changes can influence reactivity and stability of iridium catalysts for CO_2 hydrogenation and formic acid dehydrogenation. We have also determined when the secondary coordination sphere influences the activity of the catalysts (and when it does not). With iridium complexes of dxbp-type ligands as (de)hydrogenation catalysts, hydroxy groups perform better than methoxy groups when the oxyanions can form, but when hydroxy groups remain neutral, they behave similarly to methoxy substituents.

EXPERIMENTAL SECTION

General Procedures. All ligand and metal complex syntheses were performed under a nitrogen atmosphere in a glovebox or by utilizing standard Schlenk line techniques with oven-dried glassware. ^{1}H and ^{13}C NMR spectra were acquired at room temperature on a Bruker AV360 360 MHz or AV500 500 MHz spectrometer, as designated, and referenced to the solvent peak. Mid-IR spectra were collected on a Bruker Alpha ATR-IR spectrometer. Mass spectrometric data were collected on a Waters AutoSpec-Ultima NT spectrometer with electron ionization method. Elemental analyses were performed by NuMega Resonance Laboratories, Inc., San Diego, CA. Electronic spectra were measured on a PerkinElmer Lambda 35 UV−visible spectrometer. Cyclic voltammetry experiments were conducted in a 0.1 M solution of Bu_4NPF_6 in acetonitrile (MeCN) or *N*,*N*′-dimethylformamide (DMF) with a glassy carbon working electrode, a Pt counter electrode, and a Ag/AgCl reference electrode on a CHI760C Potentiostat. The redox potentials are calibrated to Fc/Fc^+ and reported vs SCE. A Fisher Scientific accumet glass electrode calibrated with standard buffer solutions was used to measure pH values. Pressurized gas reactions were performed in a Parr reaction vessel. SEM data were collected with a JEOL 7000F Field Emission Gun (FEG) for secondary and backscattered electron images. EDS data were collected using an Oxford system with Silicon Drift Detector (SDD) with Aztec software. XPS data were collected using a Kratos AXIS 165 XPS with a Mono (A1)(144W) anode, 50.0 meV step, 1000 ms dwell time, and hybrid lens mode with resolution of pass energy 20.

Materials. Dry solvents were obtained via the Glass Contour Solvent System built by Pure Process Technology, LLC. All reagents were used as purchased and degassed under vacuum as needed. The compounds 6,6′-dmbp,[62] 6,6′-dhbp,[62] [(*p*-cym)RuCl(6,6′-dmbp)]Cl ($\mathbf{5}_{Ru}$),[1] [(*p*-cym)RuCl(6,6′-dhbp)]Cl ($\mathbf{4}_{Ru}$),[1] [Cp*IrCl(6,6′-dhbp)]Cl ($\mathbf{4}_{Ir}$),[2] and [Cp*IrCl(6,6′-dmbp)]Cl[2] were prepared according to previously published procedures. High purity grade (>97%) formic acid was used as purchased from AMRESCO, Inc. The compressed gases CO_2 and 50:50 vol CO_2/H_2 were purchased from Airgas and used without further purification.

XRD Structure Determination of 1−3, $\mathbf{3}_{SP}$, $\mathbf{5}_{Ir}$, $\mathbf{5}_{Ru}$, 6, and 7. Single crystal samples of complexes **1**−**3**, $\mathbf{3}_{SP}$, $\mathbf{5}_{Ir}$, $\mathbf{5}_{Ru}$, **6**, and **7** were mounted on glass filaments on a Bruker Apex2 CCD-based X-ray diffractometer[63] equipped with an Oxford N-Helix Cryosystem at −100 °C and fine focus Mo-target X-ray tube (λ = 0.71073 Å) operated at 2000 W power (50 kV, 40 mA). The X-ray intensities were measured at 294(2) K; the detector was placed at a distance 6.000 cm from the crystal. The collected frames were integrated with the Saint[64] software package using a narrow-frame algorithm. Data were corrected for absorption effects using the multiscan method in SADABS.[65] The space group was assigned using XPREP of the Bruker ShelXTL[66] package, solved with ShelXT,[66] and refined with ShelXL[66] and the graphical interface ShelXle.[67] All non-hydrogen atoms were refined anisotropically. H atoms attached to carbon were positioned geometrically and constrained to ride on their parent atoms. Specific structure determination details are included in the Supporting Information.

Synthesis of 2-(*tert*-Butoxy)-6-(1*H*-imidazol-1-yl)pyridine (py^{O^tBu}-Im). A Schlenk flask with stir bar was loaded with KO*t*Bu (1.485 g, 13.2 mmol, 1.2 equiv) in a glovebox and sealed with a rubber septum, and THF (20 mL) was added via cannula. Under $N_{2(g)}$ atmosphere, 2,6-difluoropyridine (1.00 mL, 11.0 mmol, 1.00 equiv) was added dropwise to the stirring solution via syringe to form 2-(*tert*-butoxy)-6-fluoropyridine. This reaction was stirred for 2 h. A separate Schlenk flask with stir bar was charged with powdered sodium hydride (0.292 g, 12.2 mmol, 1.1 equiv) and anhydrous DMF (30 mL) and then sealed with a rubber septum. This reaction flask was attached to the Schlenk line and, with a positive flow of nitrogen solid imidazole (0.8257 g, 12.1 mmol, 1.1 equiv), was slowly added to the stirring suspension to form sodium imidazolate. The reaction was stirred 1 h under nitrogen until hydrogen gas ceased to evolve. The THF reaction solution prepared previously was transferred via cannula to the DMF reaction solution with stirring. With positive nitrogen flow, a reflux condenser was attached, and the flask was heated to 70 °C overnight with stirring. The reaction mixture was cooled to room temperature; the THF was removed from the mixture via a rotary evaporator, and the remaining reaction mixture was transferred to a separatory funnel with DI H_2O (300 mL). The product was extracted with CH_2Cl_2 (40 mL × 3). The organic phase was washed with brine (80 mL), dried over $MgSO_4$, and filtered; the filtrate was concentrated to dryness on a rotary evaporator, and the residue was dried under high vacuum to afford a honey-colored oil identified as desired product py^{O^tBu}-Im (2.287 g, 10.5 mmol, 95.5%). ^{1}H NMR (360 MHz, $CDCl_3$, ppm): δ 8.18 (s, 1H, Im-C*H* (N-C*H*-N)), 7.49 (t, $^3J_{HH}$ = 8.3 Hz, 1H, Py-C*H*), 7.45 (t, $^3J_{HH}$ = 1.2 Hz, 1H, Im-C*H*), 7.05 (t, $^3J_{HH}$ = 1.2 Hz, 1H, Im-C*H*), 6.74 (d, $^3J_{HH}$ = 7.8 Hz, 1H, Py-C*H*), 6.45 (d, $^3J_{HH}$ = 8.1 Hz, 1H, Py-C*H*), 1.51 (s, 9H, $OC(CH_3)_3$) (see Figure S1). ^{13}C {^{1}H}NMR (125.76 MHz, $CDCl_3$, ppm): δ 163.02 (C_{Py} (^{t}BuO-*C*═N)), 146.21 (C_{Py} (N-*C*-N)), 140.54 (C_{Py}), 134.77 (C_{Im} (N-*C*H-N)), 130.19 (C_{Im}), 115.99 (C_{Im}), 110.91 (C_{Py}), 102.84 (C_{Py}), 80.28 ($OC(CH_3)_3$), 28.41 ($OC(CH_3)_3$) (see Figure S2). FT-IR (ATR, cm^{-1}): 3114 (w), 2976 (w), 2931 (w), 1673 (m), 1603 (m), 1571 (s), 1478 (m), 1445 (vs), 1382 (m), 1364 (m), 1323 (m), 1277 (m), 1247 (m), 1232 (s), 1158 (m), 1132 (m), 1103 (m), 1056 (s), 1013 (m), 930 (m), 910 (m), 841 (m), 792 (s), 730 (m), 653 (s), 609 (w), 469 (w), 406 (w) (see Figure S4). EI-MS (EI^+): *m*/*z* found (expected): 217.1 ($[py^{OtBu}\text{-Im}]^+$ = $[C_{12}H_{15}N_3O]^+$, 217.12), 161.0 ($[py^{OH}\text{-Im}]^+$ = $[C_8H_7N_3O]^+$, 161.06) (see Figure S3).

Synthesis of 2-Methoxy-6-(1*H*-imidazol-1-yl)pyridine (py^{OMe}-Im). A Schlenk flask with stir bar was loaded with NaH (1.377g, 57.4 mmol, 1.1 equiv) and THF (250 mL) in a glovebox and then sealed with a rubber septum. Under nitrogen, anhydrous MeOH (4.23 mL, 104.4 mmol, 2.0 equiv) was added dropwise to the NaH suspension with stirring at 0 °C for 30 min until the bubbling had stopped. 2,6-Difluoropyridine (4.732 mL, 52.2 mmol, 1.0 equiv) was added dropwise to the reaction mixture via syringe. The reaction was stirred for 12 h under nitrogen at room temperature. The solvent was removed under reduced pressure. To the Schlenk flask containing crude 2-(methoxy)-6-fluoropyridine was added anhydrous DMF (250 mL) via cannula transfer. With a positive flow of nitrogen, solid imidazole (4.265 g, 62.64 mmol, 1.2 equiv) was added to the DMF solution. The reaction mixture was stirred at 0 °C for 15 min; then, with positive flow of nitrogen, NaH (1.378 g, 57.42 mmol, 1.1 equiv) was added to the reaction flask and stirred at 0 °C until the bubbling ceased. The reaction flask was allowed to warm to room temperature;

DOI: 10.1021/acs.organomet.6b00806
Organometallics 2017, 36, 1091−1106

a reflux condenser was attached, and the flask was heated overnight at 80 °C open to air. The reaction mixture was cooled to room temperature; the DMF was removed from the mixture via a rotary evaporator, and DI water (400 mL) was added to the remaining reaction mixture and then transferred to a separatory funnel. The organic phase was extracted with DCM (80 mL × 4), dried over $MgSO_4$, and filtered. The filtrate was concentrated to dryness on a rotary evaporator, and the residue was dried under high vacuum to afford a honey-colored oil identified as the desired product py^{OMe}-Im (6.003 g, 34.29 mmol, 65% yield). ^{1}H NMR (500 MHz, $CDCl_3$, ppm): δ 8.18 (s, 1H, Im-C*H* (N-C*H*-N)), 7.48 (t, $^3J_{H,H}$ = 7.9 Hz, 1H, Py-C*H*), 7.44 (t, $^3J_{H,H}$ = 1.3 Hz, 1H, Im-C*H*), 7.02 (t, $^3J_{H,H}$ = 1.1 Hz, 1H, Im-C*H*), 6.71 (d, $^3J_{H,H}$ = 7.7 Hz, 1H, Py-C*H*), 6.48 (d, $^3J_{H,H}$ = 8.2 Hz, 1H, Py-C*H*), 3.79 (s, 3H, OCH_3) (see Figure S5). ^{13}C {^{1}H}NMR (125.76 MHz, $CDCl_3$, ppm): δ 163.49 (C_{Py} (MeO-C═N)), 146.80 (C_{Py}), 140.81 (C_{Py}), 134.77 (C_{Im} (N-CH-N)), 130.27 (C_{Im}), 115.92 (C_{Im}), 108.47 (C_{Py}), 103.39 (C_{Py}), 53.43 (OCH_3) (see Figure S6). FT-IR (ATR, cm^{-1}): 3111 (w), 2982 (w), 2951 (w), 1612 (m), 1599 (m), 1578 (s), 1471 (m), 1445 (s), 1417 (m), 1376 (m), 1320 (m), 1262(m), 1247 (m), 1233 (s), 1155 (m), 1130 (m), 1102 (m), 1056 (s), 1027 (m), 990 (m), 902 (m), 855 (m), 829 (s), 788 (m), 727 (s), 671 (m), 652 (m), 608 (m), 475 (w), 449 (w) (see Figure S8). EI-MS (EI$^+$): *m*/*z* found (expected): 175.1 ([py^{OMe}-Im]$^+$ = [$C_9H_9N_3O$]$^+$, 175.07) (see Figure S7).

Synthesis of 1-(6-(*tert*-Butoxy)pyridin-2-yl)-3-methyl-1*H*-imidazol-3-ium triflate (Im^{Me}-py^{OtBu})OTf. Dry DMF (30 mL) was added via cannula to an evacuated flask containing 2-(*tert*-butoxy)-6-(1*H*-imidazol-1-yl)pyridine (2.287 g, 10.5 mmol, 1 equiv) and a stir bar. Methyl trifluoromethanesulfonate (MeOTf) (1.31 mL, 11.6 mmol, 1.1 equiv) was added dropwise with stirring at 0 °C. A white solid gradually formed with stirring. The reaction mixture was stirred for 12 h under nitrogen at room temperature. The white solid product was collected by suction filtration and washed with Et_2O. More product precipitated from the filtrate with the addition of Et_2O, which was also collected by filtration. The white solid was combined and dried under vacuum to yield the product (Im^{Me}-py^{OtBu})OTf (3.0098 g, 7.892 mmol, 75% yield). ^{1}H NMR (360 MHz, CD_3OD, ppm): δ 9.58 (broad s, 1H but integrates low due to H/D exchange with CD_3OD, Im-C*H* (N-C*H*-N)), 8.24 (d, $^3J_{HH}$ = 2.0 Hz, 1H, Im-C*H*), 7.90 (t, $^3J_{HH}$ = 8.3 Hz, 1H, Py-C*H*), 7.78 (d, $^3J_{HH}$ = 2.0 Hz, 1H, Im-C*H*), 7.37 (d, $^3J_{HH}$ = 7.9 Hz, 1H, Py-C*H*), 6.87 (d, $^3J_{HH}$ = 8.3 Hz, 1H, Py-C*H*), 4.07 (s, 3H, NCH_3), 1.66 (s, 9H, $OC(CH_3)_3$) (see Figure S9). ^{13}C {^{1}H}NMR (125.76 MHz, CD_3OD, ppm): δ 164.83 (C_{Py} (^{t}BuO-C═N)), 145.20 (C_{Py}), 143.11 (C_{Py}), 136.26 (C_{Im} (N-CH-N)), 125.91 (C_{Im}), 121.77 (q, $^1J_{CF}$ = 319.5 Hz, CF_3 of triflate), 120.49 (C_{Im}), 115.85 (C_{Py}), 106.24 (C_{Py}), 82.56 ($OC(CH_3)_3$), 37.08 (NCH_3), 28.88 ($OC(CH_3)_3$) (see Figure S10). FT-IR (ATR, cm^{-1}): 3160 (w), 3141 (w), 3119 (w), 2987 (w), 1627 (w), 1614 (w), 1565 (m), 1544 (m), 1453 (m), 1441 (m), 1368 (m), 1343 (s), 1309 (s), 1253 (s), 1220 (s), 1153 (s), 1097 (m), 1028 (s), 985 (m), 931 (m), 911 (m), 855 (m), 838 (m), 796 (m), 772 (m), 757 (m), 726 (w), 697 (w), 634 (s), 612 (m), 572 (m), 516 (s), 485 (w), 464 (w) (see Figure S12). EI-MS (EI$^+$): *m*/*z* found (expected): 232.1 ([Im^{Me}-py^{OtBu}]$^+$ = [$C_{13}H_{18}N_3O$]$^+$, 232.14), 176.1 ([Im^{Me}-py^{OH}]$^+$ = [$C_9H_{10}N_3O$]$^+$, 176.08) (see Figure S11).

Synthesis of (Im^{Me}-py^{OMe})OTf. Dry DMF (150 mL) was added via cannula to an evacuated flask containing 2-(methoxy)-6-(1*H*-imidazol-1-yl)pyridine (6.003 g, 34.28 mmol, 1 equiv) and a stir bar. Methyl trifluoromethanesulfonate (MeOTf) (4.27 mL, 37.72 mmol, 1.1 equiv) was added dropwise with stirring at 0 °C. The reaction mixture was stirred for 12 h under nitrogen at room temperature. DMF was removed via rotary evaporator to afford a honey-colored oil, which then solidified with agitation. The honey-colored solid was collected by suction filtration and washed with Et_2O (60 mL) to obtain a white solid. The solid was further dried under vacuum to yield the product (Im^{Me}-py^{OMe})OTf (12.79 g, 37.72 mmol, 72% yield). ^{1}H NMR (500 MHz, $CDCl_3$, ppm): δ 9.83 (s, 1H, Im-C*H* (N-C*H*-N)), 8.11 (t, $^3J_{HH}$ = 2.0 Hz, 1H, Im-C*H*), 7.80 (t, $^3J_{HH}$ = 8.0 Hz, 1H, Py-C*H*), 7.58 (t, $^3J_{HH}$ = 2.0 Hz, 1H, Im-C*H*), 7.41 (d, $^3J_{HH}$ = 7.8 Hz, 1H, Py-C*H*), 6.85 (d, $^3J_{HH}$ = 8.3 Hz, 1H, Py-C*H*), 4.12 (s, 3H, NCH_3), 3.98 (s, 3H, OCH_3) (see Figure S13). ^{13}C{^{1}H} NMR (125.76 MHz, $CDCl_3$, ppm): δ 163.93 (C_{Py} (MeO-C═N)), 143.69 (C_{Py}), 142.06 (C_{Py}), 134.62 (C_{Im} (N-CH-N)), 124.76 (C_{Im}), 120.63 (q, $^1J_{CF}$ = 320.1 Hz, CF_3 of triflate), 119.17 (C_{Im}), 112.64 (C_{Py}), 105.31 (C_{Py}), 54.33 (OCH_3), 36.93 (NCH_3) (see Figure S14). ^{19}F NMR (338.86 MHz, $CDCl_3$, ppm): δ −78.59 (s, CF_3 of triflate). FT-IR (ATR, cm^{-1}): 3135 (w), 3102 (w), 1626 (m), 1575 (m), 1543 (w), 1486 (m), 1448 (m), 1431 (m), 1368 (m), 1250 (s), 1223 (s), 1152 (s), 1101 (s), 1026 (s), 988 (w), 856 (w), 804 (w), 746 (w), 636 (s), 613 (m), 572 (m), 516 (m), 484 (w) (see Figure S16). EI-MS (EI$^+$): *m*/*z* found (expected): 190.1 ([Im^{Me}-py^{OMe}]$^+$ = [$C_{10}H_{12}N_3O$]$^+$, 190.10), 175.1 ([Im^{Me}-py^{OMe} − CH_3]$^+$ = [$C_9H_9N_3O$]$^+$, 175.08) (see Figure S15).

Synthesis of [Ag(NHC^{Me}-py^{OtBu})$_2$]OTf (6). An oven-dried round-bottomed Schlenk flask with stir bar was loaded with (Im^{Me}-py^{OtBu})OTf (2.007 g, 5.25 mmol, 1 equiv) and Ag_2O (0.622 g, 2.68 mmol, 0.5 equiv) in a glovebox and sealed with a rubber septum. Dry CH_2Cl_2 (45 mL) was added via cannula at the Schlenk line to make a black slurry. The flask was covered in foil to block light. Aqueous NaOH (1.3 mL, 2.6 mmol, 0.5 equiv) was added dropwise via syringe with stirring. The reaction mixture was stirred for 24 h at RT. Excess Ag_2O was removed by suction filtration over Celite, which was washed with CH_2Cl_2 (80 mL). The organic phase of the filtrate was washed with DI water (3×), dried over $MgSO_4$, and filtered, and the filtrate was concentrated to dryness. The resulting slightly colored, viscous oil was further dried under high vacuum to yield an airy white solid identified as the desired product (1.828 g, 2.54 mmol, 96.8% yield). ^{1}H NMR (360 MHz, $CDCl_3$, ppm): δ 7.67 (broad s, 1H, C*H* of the NHC), 7.55 (t, $^3J_{H,H}$ = 8.1 Hz, 1H, Py-C*H*), 7.44 (d, $^3J_{H,H}$ = 7.5 Hz, 1H, Py-C*H*), 7.31 (d, $^3J_{H,H}$ = 15.4 Hz, 1H, C*H* of the NHC), 6.69 (d, $^3J_{H,H}$ = 8.0 Hz, 1H, Py-C*H*), 4.02 (s, 3H, NCH_3), 1.57 (s, 9H, $OC(CH_3)_3$) (see Figure S17). ^{13}C {^{1}H}NMR (125.76 MHz, $CDCl_3$, ppm): δ 179.30 (C_{NHC} (carbene bound to Ag)), 163.08 (C_{Py} (MeO-C═N)), 148.44 (C_{Py}), 140.70 (C_{Py}), 123.55 (C_{NHC}), 120.84 (q, $^1J_{CF}$ = 321.4 Hz, CF_3 of triflate), 120.43 (C_{NHC}), 113.27 (C_{Py}), 107.14 (C_{Py}), 80.80 ($OC(CH_3)_3$), 39.39 (NCH_3), 28.53 ($OC(CH_3)_3$) (see Figure S18). FT-IR (ATR, cm^{-1}): 3143 (w), 3126 (w), 3084 (w), 2977 (w), 2933 (w), 1626 (w), 1607 (m), 1567 (m), 1451 (s), 1403 (m), 1403 (w), 1386 (w), 1361 (m), 1302 (w), 1257 (s), 1235 (s), 1158 (s), 1140 (s), 1029 (s), 988 (m), 927 (m), 913 (m), 844, (m), 809 (m), 794 (m), 743 (m), 636 (s), 572 (m), 516 (m), 469 (w). (see Figure S20). EI-MS (EI$^+$): *m*/*z* found (expected): 569.2 ([Ag(NHC^{Me}-py^{OtBu})$_2$]$^+$ = [$C_{26}H_{34}AgN_6O_2$]$^+$, 569.18), 512.1 ([Ag(NHC^{Me}-py^{OtBu})(NHC^{Me}-py^{O})]$^+$ = [$C_{22}H_{25}AgN_6O_2$]$^+$, 512.11) (see Figure S19). Anal. Calcd for [$C_{27}H_{34}N_6O_5F_3SAg$] = (**6**): C, 45.07%; H, 4.76%; N, 11.68%. Found: C, 44.84%; H, 4.75%; N, 11.41%.

Synthesis of [Ag(NHC^{Me}-py^{OMe})$_2$]OTf (7). In a glovebox, an oven-dried Schlenk round-bottomed flask with stir bar was loaded with (Im^{Me}-py^{OMe})OTf (3.162 g, 9.33 mmol, 1 equiv), Ag_2O (1.081 g, 4.66 mmol, 0.5 equiv), and dry CH_2Cl_2 (15 mL) forming a black slurry. The flask was covered in foil to block light. The flask was attached to the Schlenk line, and under nitrogen, aqueous NaOH (3.0 mL, 4.66 mmol, 0.5 equiv) was added dropwise via syringe with stirring. The reaction mixture was stirred for 24 h at RT. Excess Ag_2O was removed by suction filtration over Celite, which was washed with CH_2Cl_2 (30 mL). The filtrate organic phase was washed with DI water (3 times), dried over $MgSO_4$, and filtered, and the filtrate was concentrated to dryness. The resulting slightly gray colored solid was further dried under high vacuum and identified as the desired product (2.25 g, 3.55 mmol, 76.1% yield). ^{1}H NMR (360 MHz, CD_3CN, ppm): δ 7.77 (d, $^3J_{HH}$ = 1.8 Hz, 1 H, C*H* of the NHC), 7.74 (t, $^3J_{HH}$ = 7.9 Hz, 1H, Py-C*H*), 7.37 (d, $^3J_{HH}$ = 1.8 Hz, 1H, C*H* of the NHC), 7.33 (d, $^3J_{HH}$ = 7.6 Hz, 1H, Py-C*H*), 6.80 (d, $^3J_{HH}$ = 8.0 Hz, 1H, Py-C*H*), 3.94 (s, 3H, NCH_3), 3.75 (s, 3H, OCH_3) (see Figure S21). ^{13}C{^{1}H}NMR (125.76 MHz, $CDCl_3$, ppm): δ 180.30 (C_{NHC} (carbene bound to Ag), 163.90 (C_{Py} (MeO-C═N)), 149.08 (C_{Py}), 141.44 (C_{Py}), 123.69 (C_{NHC}), 121.14 (q, $^1J_{CF}$ = 320.5 Hz, CF_3 of triflate), 120.65 (C_{NHC}), 110.75 (C_{Py}), 107.68 (C_{Py}), 54.13 (OCH_3), 39.87 (NCH_3) (see Figure S22). ^{19}F NMR (338.86 MHz, $CDCl_3$, ppm): δ −78.16 (s, CF_3 of triflate) (see Figure S23). FT-IR (ATR, cm^{-1}): 3155 (w), 3131 (w), 3107 (w), 3012 (w), 2957 (w), 1602 (3), 1583 (m), 1472 (s), 1435 (m), 1270

DOI: 10.1021/acs.organomet.6b00806
Organometallics 2017, 36, 1091−1106

(s), 1237 (s), 1146 (s), 1027 (s), 980 (m), 858, (m), 791 (m), 739 (m), 717 (m), 634 (s), 571 (m), 516 (m), 469 (w). (see Figure S25). EI-HRMS (EI$^+$): m/z found (expected): 485.1 ([Ag(NHC^{Me}-py^{OMe})$_2$]$^+$ = [$C_{20}H_{22}AgN_6O_2$]$^+$, 485.09), 189.1 ([NHC^{Me}-py^{OMe}]$^+$ = [$C_{10}H_{11}N_3O$]$^+$, 189.09) (see Figure S24). Anal. Calcd for [$C_{21}H_{22}N_6O_5F_3SAg$] = (**7**): C, 39.70%; H, 3.49%; N, 13.23%. Found: C, 39.66%; H, 3.49%; N, 13.24%.

Synthesis of [Cp*IrCl(NHC^{Me}-py^{OtBu})]OTf (1). An oven-dried Schlenk flask with stir bar was loaded with [Cp*IrCl$_2$]$_2$ (0.5344 g 0.670 mmol, 1 equiv), AgOTf (0.1787 g, 0.695 mmol, 1.04 equiv), and [Ag(NHC^{Me}-py^{OtBu})$_2$]OTf (0.5006 g, 0.696 mmol, 1.04 equiv) under $N_{2(g)}$. Dry CH_2Cl_2 (50 mL) was dispensed via cannula. An immediate color change from orange to yellow was observed. The reaction mixture was stirred protected from light for 18 h, resulting in the accumulation of a tan precipitate (AgCl). The reaction mixture was filtered over Celite with suction, which was washed with CH_2Cl_2 (10 mL). The product was crystallized by layering the filtrate with Et_2O (80 mL). The resulting yellow rod crystals were collected by suction filtration and washed with ether yielding the desired product [Cp*IrCl(NHC^{Me}-py^{OtBu})]OTf (0.9341 g, 1.257 mmol, 93.7% yield). Pure microcrystalline product could also be collected by quickly adding Et_2O to the filtrate. ^{1}H NMR (360 MHz, $CDCl_3$, ppm): δ 8.14 (d, $^3J_{H,H}$ = 2.4 Hz, 1H, C*H* of the NHC), 8.01 (t, $^3J_{H,H}$ = 8.0 Hz, 1H, Py-C*H*), 7.77 (d, $^3J_{H,H}$ = 8.2 Hz, 1H, Py-C*H*), 7.34 (d, $^3J_{H,H}$ = 2.2 Hz, 1H, C*H* of the NHC), 7.03 (d, $^3J_{H,H}$ = 8.5 Hz, 1H, Py-C*H*), 4.02 (s, 3H, NCH_3), 1.73 (s, 15H, CH_3 of Cp*), 1.58 (s, 9H, (CH_3)$_3$C) (see Figure S26). ^{13}C {^{1}H}NMR (125.76 MHz, CD_3CN, ppm): δ 167.88 (C$_{NHC}$ (carbene bound to Ir), 164.92 (C$_{Py}$ (*t*BuO-C═N)), 152.28 (C$_{Py}$), 144.35 (C$_{Py}$), 126.64 (C$_{NHC}$), 122.15 (q, $^1J_{CF}$ = 321.3 Hz, CF_3 of triflate), 118.85 (C$_{NHC}$), 112.84 (C$_{Py}$), 105.35 (C$_{Py}$), 93.27 (ring *C* of Cp*), 87.45 (s, OC(CH$_3$)$_3$), 37.95 (NCH$_3$), 29.28 (OC(CH$_3$)$_3$), 9.93 (CH$_3$ of Cp*) (see Figure S27). FT-IR (ATR, cm^{-1}): 3118 (w), 2985 (w), 1619 (m), 1575 (w), 1480 (m), 1444 (m), 1399 (m), 1374 (m), 1301 (m), 1258 (s), 1222 (m), 1136 (s), 1028 (s), 910 (m), 823 (w), 800 (m), 763 (m), 717 (w), 694 (m), 636 (s), 569 (m), 514 (m), 454 (w) (see Figure S29). ESI-MS: m/z found (expected) 594.1 ([Cp*IrCl(NHC^{Me}-py^{OtBu})]$^+$ = [$C_{23}H_{32}ClIrN_3O$]$^+$, 594.19), 538.0 ([Cp*IrCl(NHC^{Me}-py^{OH})]$^+$ = [$C_{19}H_{24}ClIrN_3O$]$^+$, 538.12), 502.1 ([Cp*Ir(NHC^{Me}-py^{OH})]$^+$ = [$C_{19}H_{23}IrN_3O$]$^+$, 502.15) (see Figure S28). Anal. Calcd for [$C_{24}H_{32}N_3O_4F_3SClIr$] = (**1**): C, 38.75%; H, 4.34%; N, 5.65%. Found: C, 38.57%; H, 4.69%; N, 5.59%.

Synthesis of [Cp*IrCl(NHC^{Me}-py^{OMe})]OTf (3). The same procedure was followed as for the synthesis of [Cp*IrCl(NHC^{Me}-py^{OtBu})]OTf with the following differences. The reagents and amounts used were [Cp*IrCl$_2$]$_2$ (0.200 g 0.261 mmol, 1 equiv), AgOTf (0.0671 g, 0.261 mmol, 1 equiv), and [Ag(NHC^{Me}-py^{OMe})$_2$]OTf (0.1652 g, 0.261 mmol, 1 equiv). A color change of orange to yellow occurred with the addition of solvent. The resulting crystals that grew were yellow rods of the pure product (0.2737 g, 0.390 mmol, 75.0% yield). ^{1}H NMR (500 MHz, $CDCl_3$, ppm): δ 8.08 (d, $^3J_{HH}$ = 2.3 Hz, 1H, C*H* of the NHC), 8.04 (t, $^3J_{HH}$ = 8.2 Hz, 1H, Py-C*H*), 7.70 (d, $^3J_{HH}$ = 7.8 Hz, 1H, Py-C*H*), 7.33 (d, $^3J_{HH}$ = 2.3 Hz, 1H, C*H* of the NHC), 6.91 (d, $^3J_{HH}$ = 8.2 Hz, 1H, Py-C*H*), 4.13 (s, 3H, OCH_3), 4.03 (s, 3H, NCH_3), 1.78 (s, 15H, CH_3 of Cp*) (see Figure S35). ^{13}C {^{1}H}NMR (125.76 MHz, $CDCl_3$, ppm): δ 166.90 (C$_{NHC}$ (carbene bound to Ir), 164.43 (C$_{Py}$ (MeO-C═N)), 151.21 (C$_{Py}$), 145.21 (C$_{Py}$), 125.91 (C$_{NHC}$), 121.03 (q, $^1J_{CF}$ = 320.8 Hz, CF_3 of triflate), 118.38 (C$_{NHC}$), 104.75 (C$_{Py}$), 104.66 (C$_{Py}$), 92.61 (ring *C* of Cp*), 58.35 (OCH$_3$), 37.77 (NCH$_3$), 10.02 (CH$_3$ of Cp*) (see Figure S36). ^{19}F NMR (338.86 MHz, $CDCl_3$, ppm): δ −78.13 (s, CF_3 of triflate) (see Figure S37). FT-IR (ATR, cm^{-1}): 3107 (w), 2918 (w), 1620 (m), 1580 (w), 1488 (m), 1454 (m), 1385 (m), 1360 (m), 1299 (m), 1260 (s), 1223 (m), 1144 (s), 1058 (s), 974 (m), 794 (m), 753 (w), 694 (m), 602 (s), 571 (m), 516 (m), 479 (w) (see Figure S39). EI-MS (EI$^+$): m/z found (expected): 551.1 ([Cp*IrCl(NHC^{Me}-py^{OMe})]$^+$ = [$C_{20}H_{25}ClIrN_3O$]$^+$, 551.13), 516.2 ([Cp*Ir(NHC^{Me}-py^{OMe})]$^+$ = [$C_{20}H_{25}IrN_3O$]$^+$, 516.16) (see Figure S38). Anal. Calcd for [$C_{21}H_{26}N_3O_4F_3SClIr{\cdot}2H_2O$] = (**3**·2$H_2O$): 34.21%; H, 4.10%; N, 5.70%. Found: C, 33.93%; H, 3.92%; N, 5.68%.

Synthesis of [Cp*IrCl(NHC^{Me}-py^{OH})]OTf (2). An oven-dried round-bottomed flask with stir bar was charged with [Cp*IrCl-(NHC^{Me}-py^{OtBu})]OTf (0.1008 g, 0.136 mmol) and dry MeCN (20 mL). The solution was refluxed overnight under nitrogen. The solution was brought to room temperature and layered with dry Et_2O (100 mL). Yellow crystals were collected via suction filtration yielding the desired product [Cp*IrCl(NHC^{Me}-py^{OH})]OTf (0.0525 g, 0.0763 mmol, 56.0% yield). ^{1}H NMR (360 MHz, CD_3CN, ppm): δ 10.3 (broad s, 1H, O*H*), 7.91 (t, $^3J_{H,H}$ = 7.9 Hz, 1H, Py-C*H*), 7.80 (d, $^3J_{HH}$ = 2.2 Hz, 1H, C*H* of the NHC), 7.38 (d, $^3J_{HH}$ = 2.0 Hz, 1H, C*H* of the NHC), 7.31 (d, $^3J_{HH}$ = 7.7 Hz, 1H, Py-C*H*), 6.94 (d, $^3J_{HH}$ = 8.5 Hz, 1H, Py-C*H*), 3.96 (s, 3H, NCH_3), 1.74 (s, 15H, CH_3 of Cp*) (see Figure S30). ^{13}C{^{1}H}NMR (125.76 MHz, CD_3CN, ppm): δ 168.19 (C$_{NHC}$ (carbene bound to Ir), 165.00 (C$_{Py}$ (HO-C═N)), 151.66 (C$_{Py}$), 144.71 (C$_{Py}$), 126.70 (C$_{NHC}$), 122.03 (q, $^1J_{CF}$ = 321.0 Hz, CF_3 of triflate), ∼118.31 (C$_{NHC}$ peak appears to be under the solvent peak), 109.02 (C$_{Py}$), 103.34 (C$_{Py}$), 93.49 (ring *C* of Cp*), 38.41 (NCH$_3$), 10.17 (CH$_3$ of Cp*) (see Figure S31). ^{19}F NMR (338.86 MHz, CD_3CN, ppm): δ −79.34 (s, CF_3 of triflate). FT-IR (ATR, cm^{-1}): 3101 (w), 2917 (w), 2799 (w),1626 (m), 1582 (m), 1485 (m), 1472 (m), 1400 (w), 1323 (w), 1294 (m), 1229 (s), 1213 (m), 1176 (m), 1151 (m), 1020 (s), 884 (w), 804 (m), 745 (m), 719 (m), 693 (m), 633 (s), 604 (m), 514 (m), 486 (w), 436 (w) (see Figure S33). EI-MS (EI$^+$): m/z found (expected): 537.1 ([Cp*IrCl(NHC^{Me}-py^{OH})]$^+$ = [$C_{19}H_{23}ClIrN_3O$]$^+$, 537.12), 501.1 ([Cp*Ir(NHC^{Me}-py^{OH})]$^+$ = [$C_{19}H_{23}IrN_3O$]$^+$, 501.15), 651.2 ([Cp*Ir(NHC^{Me}-py^{OH})(OTf)]$^+$ = [$C_{20}H_{23}F_3IrN_3O_4S$]$^+$, 651.10) (see Figure S32). Anal. Calcd for [$C_{20}H_{24}N_3O_4F_3SClIr{\cdot}H_2O$] = (**2**·$H_2O$): C, 34.06%; H, 3.72%; N, 5.96%. Found: C, 34.42%; H, 3.79%; N, 5.91%.

Synthesis of [Cp*IrCl(6,6′-dmbp)]OTf (5_{Ir}). A similar procedure was followed as for the synthesis of [Cp*IrCl(NHC^{Me}-py^{OtBu})]OTf with the following differences. The regents and amounts used were [Cp*IrCl$_2$]$_2$ (0.1416 g 0.178 mmol, 1 equiv), AgOTf (0.0951 g, 0.370 mmol, 2.08 equiv), and 6,6′-dmbp (0.0801 g, 0.370 mmol, 2.08 equiv). A color change of orange to yellow occurred with the addition of solvent. The reaction mixture was concentrated to dryness after filtering, and the desired product was collected as a yellow powder, which was recrystallized from MeCN solution and layered with dry Et_2O (0.2458 g, 0.338 mmol, 94.9% yield). ^{1}H NMR (360 MHz, CD_3CN, ppm): δ 8.12 (t, $^3J_{H,H}$ = 8.4 Hz, 2H, Py-C*H*), 7.95 (d, $^3J_{H,H}$ = 7.7 Hz, 2H, Py-C*H*), 7.26 (d, $^3J_{H,H}$ = 8.5 Hz, 2H, Py-C*H*), 4.10 (s, 6H, OCH_3), 1.53 (s, 15H, CH_3 of Cp*) (see Figure S40). ^{13}C {^{1}H}NMR (125.76 MHz, CD_3CN, ppm): δ 165.43 (C$_{Py}$ (MeO-C═N)), 155.55 (C$_{Py}$), 144.02 (C$_{Py}$), ∼118 (peaks for CF_3 carbon are very weak), 117.65 (C$_{Py}$), 110.91 (C$_{Py}$), 90.01 (ring *C* of Cp*), 58.65 (OCH$_3$), 9.75 (CH$_3$ of Cp*) (see Figure S41). ^{19}F NMR (338.86 MHz, CD_3CN, ppm): δ −79.33 (s, CF_3 of triflate) (see Figure S42). FT-IR (ATR, cm^{-1}): 441 (w), 463 (w), 515 (m), 570 (m), 634 (s), 681 (w), 711 (w), 743 (w), 797 (s), 814 (w), 1028 (s), 1074 (m), 1142 (s), 1194 (w), 1222 (m), 1255 (s), 1276 (m), 1303 (w), 1349 (w), 1425 (w), 1484 (m), 1572 (m), 1603 (m), 2856 (w), 3075 (w) (see Figure S44). ESI-MS: m/z found (expected): 579.1 ([Cp*IrCl(6,6′-dmbp)]$^+$ = [$C_{22}H_{27}ClIrN_2O_2$]$^+$, 579.14), 543.1 ([Cp*Ir(6,6′-dmbp)]$^+$ = [$C_{22}H_{26}IrN_2O_2$]$^+$, 543.16) (see Figure S43). Anal. Calcd for [$C_{23}H_{27}N_2O_5F_3SClIr$] = ($\mathbf{5_{Ir}}$): C, 37.91%; H, 3.74%; N, 3.85%. Found: C, 37.95%; H, 3.81%; N, 3.77%.

Procedure for Catalytic Hydrogenation of CO_2. Catalyst solution (0.3 mM, 25 mL) in 1 M $NaHCO_{3(aq)}$ was added to a Parr high-pressure vessel. The vessel was purged at least 3 times and then pressurized to 300 psig with 50:50 CO_2/H_2. The vessel was heated at 115 °C with stirring for 18 h. After the reaction time, the vessel was cooled to room temperature, and the pressure was released. The amount of formate produced was determined by ^{1}H NMR spectroscopy in D_2O with isonicotinic acid as an internal standard.

Halide Removal in Situ for Hydrogenation. Silver triflate (1 equiv for catalysts of formula [Cp*IrCl(L)]OTf and 2 equiv for catalysts with formula [Cp*IrCl(L)]Cl and [(*p*-cym)RuCl(L)]Cl) was added to the freshly prepared stock solution of aqueous catalyst (0.3 mM, 50 mL) and allowed to stir at room temperature in the absent of light for at least 6 h. The reaction mixture was filtered over Celite with suction.

DOI: 10.1021/acs.organomet.6b00806
Organometallics 2017, 36, 1091−1106

A 25 mL portion of the filtrate was used without further characterization according to the catalytic hydrogenation procedure previously stated.

Procedure for Catalytic Dehydrogenation of Formic Acid. A stock solution of catalyst (0.3 mM, 100 mL) was freshly prepared in water. Three simultaneous trials were run by transferring 25 mL (0.075 mmol, ~ 0.003 mol % catalytic loading) of stock solution to three separate 100 mL Schlenk flasks each with tubing to an upturned water filled graduated cylinder in a water basin. The reaction flasks were heated to constant temperature of 60 °C with stirring, and high purity formic acid (1.00 mL, 26.5 mmol) was added to each reaction flask. The dehydrogenation reactions were monitored for 3 h for all reactions and for longer times as indicated. The evolved gas was measured, and the TON was calculated based on the number of moles of the catalyst used divided by the moles of CO_2 produced (calculated as one-half of the total volume of gas generated and assuming the ideal gas law).

Halide removal in situ for dehydrogenation. Silver triflate (1 equiv for catalysts of formula [Cp*IrCl(L)]OTf and 2 equiv for catalysts with formula [Cp*IrCl(L)]Cl and [(*p*-cym)RuCl(L)]Cl) was added to the freshly prepared stock solution of aqueous catalyst (0.3 mM, 100 mL) and allowed to stir at room temperature in the absent of light. After 12 h of stirring, the reaction mixture was filtered over Celite with suction and used without further characterization according to the catalytic dehydrogenation procedure previously stated.

Computational Methods. The mechanisms were proposed via DFT computations using Gaussian 09 (revision E01).[68] Gas phase geometry optimizations were carried out with PBEPBE[69,70] functional and basis set 1 (BS1). In BS1, iridium utilized the Couty and Hall modified-LANL2DZ[71−73] basis set and the associated LANL2DZ effective core potential, and all other atoms (C, O, N, Na, and H) used the 6-31G (*d*′)[74−77] basis sets. Harmonic vibrational frequency computations were performed to verify the nature of all stationary points. For the solvation effect in aqueous conditions to be approximated, the self-consistent reaction field (SCRF) single-point computations with the SMD solvation model[78] on gas-phase optimized geometries were performed. Nondefault self-consistent field (SCF) convergence (10^{-6}) and density fitting approximation (with AUTO keyword)[79,80] were used in geometry optimizations and single-point SMD solvation computations. Spherical harmonic 5*d* and 7*f* functions and a pruned integration grid containing 75 radial shells and 302 angular points per shell were used for all computations. Free energy corrections were determined at 1 atm and 298.15 K. The experimental value of proton solvation energy in water (−265.9 kcal mol^{-1})[81,82] and experimental Gibbs free energy of proton (−6.28 kcal mol^{-1})[83,84] were used to calculate the relative reaction energy of the proposed mechanisms.

■ ASSOCIATED CONTENT

Supporting Information

The Supporting Information is available free of charge on the ACS Publications website at DOI: 10.1021/acs.organomet.6b00806.

Further experimental details for the synthesis, characterization, and cyclic voltammetry studies where available on all compounds described herein; studies of the transformations of the catalysts under hydrogenation and dehydrogenation conditions; computational details and energies; the atomic coordinates for these structures have also been deposited with the Cambridge Crystallographic Data Centre as CCDC 1474360−1474366 and 1509424. (PDF)

Optimized Cartesian coordinates (XYZ)

Crystallographic information (CIF)

■ AUTHOR INFORMATION

Corresponding Authors

*E-mail: dbgrotjahn@mail.sdsu.edu.

*E-mail: ewebster@chemistry.msstate.edu.

*E-mail: etpapish@ua.edu.

ORCID

Fengrui Qu: 0000-0002-9975-2573

Robert M. Vasquez: 0000-0002-6921-7764

Douglas B. Grotjahn: 0000-0002-2481-7889

Charles Edwin Webster: 0000-0002-6917-2957

Elizabeth T. Papish: 0000-0002-7937-8019

Notes

The authors declare no competing financial interest.

■ ACKNOWLEDGMENTS

We thank NSF CAREER for past support (Grants CHE-0846383 and CHE-1360802 to E.T.P. and her group), NSF EPSCoR Track 2 Seed Grant to E.T.P. for support during 2016 (PI N. Hammer, Grant OIA-1539035), Drexel University for past support, and the University of Alabama for generous financial support (including a UCRA award to N.C. and CARSCA support). Computational work was partially supported by the Mississippi State University Office of Research and Economic Development and the National Science Foundation (OIA-1539035). Computations were performed at the Mississippi State University High Performance Computing Collaboratory and the Mississippi Center for Supercomputing Research. D.B.B thanks a GAANN program fellowship (Grant P200A150329). R.M.V. thanks the NIH SDSU IMSD Program Grant GM058906-16. We also thank Qiaoli Liang (the University of Alabama) for MS analysis. Finally, we thank the members of the Papish group for assistance and suggestions. We thank Nicholas J. White for early work on this project. We thank Matthias Zeller (Purdue University) and Allen Oliver (Notre Dame) for help with X-ray structure determination. We thank Johnny R. Goodwin for SEM and Rob Holler and Tabitha Sutch for XPS experiment assistance.

■ REFERENCES

(1) Nieto, I.; Livings, M. S.; Sacci, J. B.; Reuther, L. E.; Zeller, M.; Papish, E. T. *Organometallics* **2011**, *30*, 6339−6342.

(2) DePasquale, J.; Nieto, I.; Reuther, L. E.; Herbst-Gervasoni, C. J.; Paul, J. J.; Mochalin, V.; Zeller, M.; Thomas, C. M.; Addison, A. W.; Papish, E. T. *Inorg. Chem.* **2013**, *52*, 9175−9183.

(3) Marelius, D. C.; Bhagan, S.; Charboneau, D. J.; Schroeder, K. M.; Kamdar, J. M.; McGettigan, A. R.; Freeman, B. J.; Moore, C. E.; Rheingold, A. L.; Cooksy, A. L.; Smith, D. K.; Paul, J. J.; Papish, E. T.; Grotjahn, D. B. *Eur. J. Inorg. Chem.* **2014**, *2014*, 676−689.

(4) Gerlach, D. L.; Bhagan, S.; Cruce, A. A.; Burks, D. B.; Nieto, I.; Truong, H. T.; Kelley, S. P.; Herbst-Gervasoni, C. J.; Jernigan, K. L.; Bowman, M. K.; Pan, S.; Zeller, M.; Papish, E. T. *Inorg. Chem.* **2014**, *53*, 12689−12698.

(5) Fujita, K.-i.; Kawahara, R.; Aikawa, T.; Yamaguchi, R. *Angew. Chem.* **2015**, *127*, 9185−9188.

(6) Wang, W.-H.; Hull, J. F.; Muckerman, J. T.; Fujita, E.; Himeda, Y. *Energy Environ. Sci.* **2012**, *5*, 7923−7926.

(7) Lewandowska-Andralojc, A.; Polyansky, D. E.; Wang, C.-H.; Wang, W.-H.; Himeda, Y.; Fujita, E. *Phys. Chem. Chem. Phys.* **2014**, *16*, 11976−11987.

(8) Zhang, T.; deKrafft, K. E.; Wang, J.-L.; Wang, C.; Lin, W. *Eur. J. Inorg. Chem.* **2014**, *2014*, 698−707.

DOI: 10.1021/acs.organomet.6b00806
Organometallics 2017, 36, 1091−1106

(9) Wang, W.-H.; Xu, S.; Manaka, Y.; Suna, Y.; Kambayashi, H.; Muckerman, J. T.; Fujita, E.; Himeda, Y. *ChemSusChem* **2014**, *7*, 1976−1983.
(10) Fujita, K.-i.; Tanaka, Y.; Kobayashi, M.; Yamaguchi, R. *J. Am. Chem. Soc.* **2014**, *136*, 4829−4832.
(11) Hull, J. F.; Himeda, Y.; Wang, W.-H.; Hashiguchi, B.; Periana, R.; Szalda, D. J.; Muckerman, J. T.; Fujita, E. *Nat. Chem.* **2012**, *4*, 383−388.
(12) Tanaka, R.; Yamashita, M.; Nozaki, K. *J. Am. Chem. Soc.* **2009**, *131*, 14168−14169.
(13) Kang, P.; Cheng, C.; Chen, Z.; Schauer, C. K.; Meyer, T. J.; Brookhart, M. *J. Am. Chem. Soc.* **2012**, *134*, 5500−5503.
(14) Ahn, S. T.; Bielinski, E. A.; Lane, E. M.; Chen, Y.; Bernskoetter, W. H.; Hazari, N.; Palmore, G. T. R. *Chem. Commun.* **2015**, *51*, 5947−5950.
(15) Wang, W.-H.; Himeda, Y.; Muckerman, J. T.; Manbeck, G. F.; Fujita, E. *Chem. Rev.* **2015**, *115*, 12936−12973.
(16) Celaje, J. J. A.; Lu, Z.; Kedzie, E. A.; Terrile, N. J.; Lo, J. N.; Williams, T. J. *Nat. Commun.* **2016**, *7*, 11308−11313.
(17) Bielinski, E. A.; Förster, M.; Zhang, Y.; Bernskoetter, W. H.; Hazari, N.; Holthausen, M. C. *ACS Catal.* **2015**, *5*, 2404−2415.
(18) Hu, P.; Diskin-Posner, Y.; Ben-David, Y.; Milstein, D. *ACS Catal.* **2014**, *4*, 2649−2652.
(19) Hu, Y.; Shaw, A. P.; Guan, H.; Norton, J. R.; Sattler, W.; Rong, Y. *Organometallics* **2016**, *35*, 39−46.
(20) Hu, Y.; Norton, J. R. *J. Am. Chem. Soc.* **2014**, *136*, 5938−5948.
(21) Hu, Y.; Li, L.; Shaw, A. P.; Norton, J. R.; Sattler, W.; Rong, Y. *Organometallics* **2012**, *31*, 5058−5064.
(22) Hu, Y.; Shaw, A. P.; Estes, D. P.; Norton, J. R. *Chem. Rev.* **2016**, *116*, 8427−8462.
(23) Fagan, P. J.; Voges, M. H.; Bullock, R. M. *Organometallics* **2010**, *29*, 1045−1048.
(24) Ledger, A. E. W.; Moreno, A.; Ellul, C. E.; Mahon, M. F.; Pregosin, P. S.; Whittlesey, M. K.; Williams, J. M. J. *Inorg. Chem.* **2010**, *49*, 7244−7256.
(25) Namorado, S.; Antunes, M. A.; Veiros, L. F.; Ascenso, J. R.; Duarte, M. T.; Martins, A. M. *Organometallics* **2008**, *27*, 4589−4599.
(26) Guan, H.; Iimura, M.; Magee, M. P.; Norton, J. R.; Zhu, G. *J. Am. Chem. Soc.* **2005**, *127*, 7805−7814.
(27) Papish, E. T.; Magee, M. P.; Norton, J. R. *in Recent Advances in Hydride Chemistry published by Elsevier* **2001**, 39−74.
(28) Casey, C. P.; Guan, H. *J. Am. Chem. Soc.* **2009**, *131*, 2499−2507.
(29) Casey, C. P.; Johnson, J. B.; Singer, S. W.; Cui, Q. *J. Am. Chem. Soc.* **2005**, *127*, 3100−3109.
(30) Casey, C. P.; Singer, S. W.; Powell, D. R.; Hayashi, R. K.; Kavana, M. *J. Am. Chem. Soc.* **2001**, *123*, 1090−1100.
(31) Shvo, Y.; Czarkie, D.; Rahamim, Y.; Chodosh, D. F. *J. Am. Chem. Soc.* **1986**, *108*, 7400−7402.
(32) Arduengo, A. J. *Acc. Chem. Res.* **1999**, *32*, 913−921.
(33) Ledoux, N.; Allaert, B.; Linden, A.; Van Der Voort, P.; Verpoort, F. *Organometallics* **2007**, *26*, 1052−1056.
(34) Dharmasena, U. L.; Foucault, H. M.; dos Santos, E. N.; Fogg, D. E.; Nolan, S. P. *Organometallics* **2005**, *24*, 1056−1058.
(35) Danopoulos, A. A.; Pugh, D.; Smith, H.; Saßmannshausen, J. *Chem. - Eur. J.* **2009**, *15*, 5491−5502.
(36) Chen, H.-S.; Chang, W.-C.; Su, C.; Li, T.-Y.; Hsu, N.-M.; Tingare, Y. S.; Li, C.-Y.; Shie, J.-H.; Li, W.-R. *Dalton Trans.* **2011**, *40*, 6765−6770.
(37) Specht, Z. G.; Grotjahn, D. B.; Moore, C. E.; Rheingold, A. L. *Organometallics* **2013**, *32*, 6400−6409.
(38) Huckaba, A. J.; Sharpe, E. A.; Delcamp, J. H. *Inorg. Chem.* **2016**, *55*, 682−690.
(39) Stanton, I.; Charles, J.; Machan, C. W.; Vandezande, J. E.; Jin, T.; Majetich, G. F.; Schaefer, I.; Henry, F.; Kubiak, C. P.; Li, G.; Agarwal, J. *Inorg. Chem.* **2016**, *55*, 3136−3144.
(40) Agarwal, J.; Shaw, T. W.; Stanton, I.; Charles, J.; Majetich, G. F.; Bocarsly, A. B.; Schaefer, I.; Henry, F. *Angew. Chem., Int. Ed.* **2014**, *53*, 5152−5155.
(41) Thoi, V. S.; Kornienko, N.; Margarit, C. G.; Yang, P.; Chang, C. J. *J. Am. Chem. Soc.* **2013**, *135*, 14413−14424.
(42) Brioche, J.; Michalak, M.; Quiclet-Sire, B.; Zard, S. Z. *Org. Lett.* **2011**, *13*, 6296−6299.
(43) Gronnier, C.; Bel, P. F. d.; Henrion, G.; Kramer, S.; Gagosz, F. *Org. Lett.* **2014**, *16*, 2092−2095.
(44) Schlosser, M.; Rausis, T. *Helv. Chim. Acta* **2005**, *88*, 1240−1249.
(45) Wang, H. M. J.; Lin, I. J. B. *Organometallics* **1998**, *17*, 972−975.
(46) Gerlach, D. L.; Nieto, I.; Herbst-Gervasoni, C. J.; Ferrence, G. M.; Zeller, M.; Papish, E. T. *Acta Cryst. Section E* **2015**, *71*, 1447−1453.
(47) Specht, Z. G.; Cortes-Llamas, S. A.; Tran, H. N.; van Niekerk, C. J.; Rancudo, K. T.; Golen, J. A.; Moore, C. E.; Rheingold, A. L.; Dwyer, T. J.; Grotjahn, D. B. *Chem. - Eur. J.* **2011**, *17*, 6606−6609.
(48) Zhang, T.; Wang, C.; Liu, S.; Wang, J.-L.; Lin, W. *J. Am. Chem. Soc.* **2014**, *136*, 273−281.
(49) Himeda, Y. *Eur. J. Inorg. Chem.* **2007**, *2007*, 3927−3941.
(50) Campos, J.; Hintermair, U.; Brewster, T. P.; Takase, M. K.; Crabtree, R. H. *ACS Catal.* **2014**, *4*, 973−985.
(51) Ghorai, D.; Dutta, C.; Choudhury, J. *ACS Catal.* **2016**, *6*, 709−713.
(52) Cocco, F.; Cinellu, M. A.; Minghetti, G.; Zucca, A.; Stoccoro, S.; Maiore, L.; Manassero, M. *Organometallics* **2010**, *29*, 1064−1066.
(53) Moore, C. M.; Bark, B.; Szymczak, N. K. *ACS Catal.* **2016**, *6*, 1981−1990.
(54) Dub, P. A.; Henson, N. J.; Martin, R. L.; Gordon, J. C. *J. Am. Chem. Soc.* **2014**, *136*, 3505−3521.
(55) Hartmann, R.; Chen, P. *Angew. Chem., Int. Ed.* **2001**, *40*, 3581−3585.
(56) John, J. M.; Takebayashi, S.; Dabral, N.; Miskolzie, M.; Bergens, S. H. *J. Am. Chem. Soc.* **2013**, *135*, 8578−8584.
(57) Hayes, J. M.; Deydier, E.; Ujaque, G.; Lledós, A.; Malacea-Kabbara, R.; Manoury, E.; Vincendeau, S.; Poli, R. *ACS Catal.* **2015**, *5*, 4368−4376.
(58) O, W. W. N.; Lough, A. J.; Morris, R. H. *Organometallics* **2012**, *31*, 2152−2165.
(59) Ertem, M. Z.; Himeda, Y.; Fujita, E.; Muckerman, J. T. *ACS Catal.* **2016**, *6*, 600−609.
(60) Moore, C. M.; Dahl, E. W.; Szymczak, N. K. *Curr. Opin. Chem. Biol.* **2015**, *25*, 9−17.
(61) Moore, C. M.; Szymczak, N. K. *Chem. Commun.* **2013**, *49*, 400−402.
(62) Dubreuil, D. M.; Pipelier, M. G.; Pradere, J. P.; Bakkali, H.; Lepape, P.; Delaunay, T.; Tabatchnik, A. *Pyridine and Pyrrole Compounds, Processes for Obtaining Them and Uses*; World patent: WO 2008/012440 A2, 2008.
(63) Bruker *Apex2* 2013.10-0; Bruker AXS Inc.: Madison, Wisconsin, USA, 2007.
(64) Bruker *Saint Plus*, 8.34A; Bruker AXS Inc.: Madison, Wisconsin, USA, 2007.
(65) Bruker *SADABS*, 2012/1; Bruker AXS Inc.: Madison, Wisconsin, USA, 2001.
(66) Sheldrick, G. M. *Acta Crystallogr., Sect. A: Found. Crystallogr.* **2008**, *64*, 112−122.
(67) Hübschle, C. B.; Sheldrick, G. M.; Dittrich, B. *J. Appl. Crystallogr.* **2011**, *44*, 1281−1284.
(68) Frisch, M. J.; Trucks, G. W.; Schlegel, H. B.; Scuseria, G. E.; Robb, M. A.; Cheeseman, J. R.; Scalmani, G.; Barone, V.; Mennucci, B.; Petersson, G. A.; Nakatsuji, H.; Caricato, M.; Li, X.; Hratchian, H. P.; Izmaylov, A. F.; Bloino, J.; Zheng, G.; Sonnenberg, J. L.; Hada, M.; Ehara, M.; Toyota, K.; Fukuda, R.; Hasegawa, J.; Ishida, M.; Nakajima, T.; Honda, Y.; Kitao, O.; Nakai, H.; Vreven, T.; Montgomery, J. A., Jr.; Peralta, J. E.; Ogliaro, F.; Bearpark, M. J.; Heyd, J.; Brothers, E. N.; Kudin, K. N.; Staroverov, V. N.; Kobayashi, R.; Normand, J.; Raghavachari, K.; Rendell, A. P.; Burant, J. C.; Iyengar, S. S.; Tomasi, J.; Cossi, M.; Rega, N.; Millam, N. J.; Klene, M.; Knox, J. E.; Cross, J. B.; Bakken, V.; Adamo, C.; Jaramillo, J.; Gomperts, R.; Stratmann, R. E.; Yazyev, O.; Austin, A. J.; Cammi, R.; Pomelli, C.; Ochterski, J. W.; Martin, R. L.; Morokuma, K.; Zakrzewski, V. G.;

DOI: 10.1021/acs.organomet.6b00806
Organometallics 2017, 36, 1091−1106

Voth, G. A.; Salvador, P.; Dannenberg, J. J.; Dapprich, S.; Daniels, A. D.; Farkas, Ö.; Foresman, J. B.; Ortiz, J. V.; Cioslowski, J.; Fox, D. J. *Gaussian 09*, revision E.01; Gaussian, Inc.: Wallingford, CT, USA, 2013.
(69) Perdew, J. P.; Burke, K.; Ernzerhof, M. *Phys. Rev. Lett.* **1996**, *77*, 3865−3868.
(70) Perdew, J. P.; Burke, K.; Ernzerhof, M. *Phys. Rev. Lett.* **1997**, *78*, 1396.
(71) Couty, M.; Hall, M. B. *J. Comput. Chem.* **1996**, *17*, 1359−1370.
(72) Hay, P. J.; Wadt, W. R. *J. Chem. Phys.* **1985**, *82*, 270−283.
(73) Hay, P. J.; Wadt, W. R. *J. Chem. Phys.* **1985**, *82*, 299−310.
(74) Hehre, W. J.; Ditchfield, R.; Pople, J. A. *J. Chem. Phys.* **1972**, *56*, 2257−2261.
(75) Hariharan, P. C.; Pople, J. A. *Theor. Chim. Acta* **1973**, *28*, 213−222.
(76) Foresman, J. B.; Frisch, A. E. *Exploring Chemistry with Electronic Structure Methods*, 2nd ed.; Gaussian, Inc: Pittsburgh, PA, 1996; p 110.
(77) The 6-31G(d′) basis set has the d polarization functions for C, N, and O taken from the 6-311G(d) basis sets instead of the original arbitrarily assigned value of 0.8 used in the 6-31G(d) basis sets.
(78) Marenich, A. V.; Cramer, C. J.; Truhlar, D. G. *J. Phys. Chem. B* **2009**, *113*, 6378−6396.
(79) Dunlap, B. I. *J. Chem. Phys.* **1983**, *78*, 3140−3142.
(80) Dunlap, B. I. *J. Mol. Struct.: THEOCHEM* **2000**, *529*, 37−40.
(81) Camaioni, D. M.; Schwerdtfeger, C. A. *J. Phys. Chem. A* **2005**, *109*, 10795−10797.
(82) Kelly, C. P.; Cramer, C. J.; Truhlar, D. G. *J. Phys. Chem. B* **2006**, *110*, 16066−16081.
(83) Fifen, J. J.; Dhaouadi, Z.; Nsangou, M. J. *J. Phys. Chem. A* **2014**, *118*, 11090−11097.
(84) Moser, A.; Range, K.; York, D. M. *J. Phys. Chem. B* **2010**, *114*, 13911−13921.

DOI: 10.1021/acs.organomet.6b00806
Organometallics 2017, 36, 1091−1106